NASA Contractor Report 4101

Transonic Analysis and Design of Axisymmetric Bodies in Nonuniform Flow

Jen-Fu Chang and C. Edward Lan

The University of Kansas Center for Research, Inc.
Lawrence, Kansas

NASA

National Aeronautics
and Space Administration

Scientific and Technical
Information Division

1987

SUMMARY

An inviscid nonuniform axisymmetric transonic code is developed
for applications in analysis and design. Propfan slipstream effect
on pressure distribution for a body with and without sting is
investigated. Results show that nonuniformity causes pressure
coefficient to be more negative and shock strength to be stronger
and more rearward. Sting attached to a body reduces the pressure
peak and moves the rear shock forward. Extent and Mach profile
shapes of the nonuniformity region appear to have little effect on
the pressure distribution. Increasing nonuniformity magnitude makes
pressure coefficient more negative and moves the shock rearward.

Design study is conducted with the CONMIN optimizer for an
ellipsoid and a body with the NACA-0012 contour. For the ellipsoid,
the general trend shows that to reduce the pressure drag, the front
portion of the body should be thinner and the contour of the rear
portion should be flatter than the ellipsoid. In a uniform flow of
Mach number equal to 1.1, a reduction in pressure drag of 14 percent
is achieved; while at a Mach number of 0.995, only 5 percent in drag
reduction is possible. In a nonuniform flow of Mach number 0.995 to
1.1, a drag reduction of 13 percent is obtained. For the design of
a body with a sharp trailing edge in transonic flow with an initial
shape given by the NACA 0012 contour, the pressure drag is reduced
by decreasing the nose radius and increasing the thickness in the
aft portion. Drag reduction achieved in a uniform flow of Mach
number equal to 0.98 is 46 percent; in a nonuniform flow of Mach
number equal to 0.98 to 0.995, 29 percent.

i

TABLE OF CONTENTS

LIST OF SYMBOLS

a	Local speed of sound
a_1, a_2, a_3, a_4	Coefficients in the stretching function
A	Parameter of physical step size at the body
A	Constant in defining the stretching function
A_i	Coefficients in the Fourier sine series
b	Derivative of the stretching function at $x = x_m$
B	Constant in defining the stretching function
c	Reference length
c_1, c_2, c_3	Coefficients in defining the stretching function
c_{d_w}, c_d	Pressure drag coefficient based on maximum radius squared
C_p	Pressure coefficient
f	Derivative of the stretching function in the ξ direction
F	Rotation function
g	Derivative of the stretching function in the η direction
G	Constraint function
h_1, h_2, h_3	Metrics of x_1, x_2, and x_3 coordinates
H	$= 1 + \kappa\eta$, metric of the x_1 coordinate
i	Index for the x_1 or ξ direction
j	Index for the x_2 or η direction
$\vec{k}$	Unit vector in the ζ direction
ℓ	Body length
M	Mach number

N	Normal direction of a streamline, or number of Fourier sine series
OBJ	Objective function
P	Pressure
$\vec{q}$	Local velocity vector
r	Radius from the symmetry axis
R	Nondimensional gas constant
r_b	Body radius
r_b'	First derivative of the local body radius
r_b''	Second derivative of the local body radius
S	Streamline direction on a streamline
T	Temperature
u	x_1 component of the velocity vector $\vec{q}$
v	x_2 component of the velocity vector $\vec{q}$
w	x_3 component of the velocity vector $\vec{q}$
x	Horizontal axis on the transformed plane
x_1, x_2, x_3	Coordinates in the curvilinear coordinate system
x_i	Starting x coordinate
x_ℓ	Ending x coordinate

Greek

α	Parameter controlling the size of the last finite value
γ	Ratio of specific heats
Δ	Difference operator

LIST OF SYMBOLS, continued

ϕ	Velocity function
μ	Index
κ	Curvature of the reference coordinator surface
ψ	Stream function
∇	Del (gradient) operator
ρ	Local density
θ	Angle of the reference coordinate surface with respect to the horizontal line, or angle associated with Fourier series
τ	Stretch function in the ξ direction
$\vec{\omega}$	Vorticity vector
ξ	Tangential axis of the body normal coordinate
η	Normal axis of the body normal coordinate
ζ	Symmetry axis of the body normal coordinate

Subscripts

a	Ambient quantity, or quantity on the symmetry axis
B	Body surface
inf	Far field quantity
jmax	Index at the body surface in the normal direction
ℓe	Leading edge
lower	Lower constraints
max	Maximum quantity
o	Quantity on the axis or at the nose, or stagnation quantity

LIST OF SYMBOLS, continued

ref	Reference quantity
te	Trailing edge
upper	Upper constraints
∞	Far field quantity
η	Normal direction of the body coordinate
ξ	Tangential direction of the body coordinate

Abbreviations

CONMIN	CONstrained MINimization
CPU	Central Processing Unit
RAXBOD	Relaxation for AXisymmetric BODies

1. INTRODUCTION

Typical transonic axisymmetric nonuniform flows include propfan flow around a nacelle and a center body immersed in a jet. By introducing a rotation function to account for nonuniformity effects, a potential-like equation can be derived from the Euler equation, valid along a streamline. Therefore, the problem can be solved by revising an existing full-potential code, such as Reference 1. This idea was used by Brown (Ref. 2) in the transonic axisymmetric nozzle problem. The same formulation is presented in Reference 3 for an airfoil in a nonuniform flow. In both cases, a total velocity function is used as the primary variable.

Optimal axisymmetric shapes have been sought experimentally by Whitcomb (Ref. 4) for subsonic free stream. Based on a slender body theory, von Karman's ogive (Ref. 5) and Sears-Haack body (Refs. 6 and 7) can be analytically derived. Chan (Ref. 8) coupled a transonic small-disturbance code (Ref. 9) with a simplex optimizer (Ref. 10) to determine numerically optimized shapes at uniform free-stream Mach numbers of .98 and 1.1. However, the transonic small-disturbance equation is not appropriate for computation of drag for shapes of the blunt-nose type frequently used at transonic speeds. Optimal shapes in axisymmetric nonuniform transonic flow have not been investigated in the past.

In this paper, a method based on disturbance potential-like equation is presented to solve the nonuniform, axisymmetric transonic problem. It is suitable for subsonic to low supersonic

1

nonuniform flow and shapes of the blunt-nose type. Optimal shapes
with minimum pressure drag will be sought by coupling analysis with
an optimizer (Ref. 13), using the maximum thickness and the trailing
edge closure as constraints. Effects of different Mach number
nonuniformity and profile shapes will also be investigated.

2. THEORETICAL DEVELOPMENT

2.1 Governing Equations for Axisymmetric Nonuniform Flow

The steady Euler equation along a streamline is (by combining Equations 1, 2, and 5 in Reference 3)

$$a^2 \, \nabla \cdot \vec{q} = \frac{1}{2} \, \vec{q} \cdot \nabla |\vec{q}|^2 \qquad (1)$$

where a is the local speed of sound and $\vec{q}$ is the local velocity vector. To satisfy the surface boundary conditions exactly, the body-normal coordinates are used in the nose region to fit the blunt nose, and sheared cylindrical coordinates are used on the afterbody to accommodate corners such as boattails and flares (Ref. 11). For smooth, closed, convex bodies which are blunt on both ends, the transformed coordinates (ξ, η) are chosen to be the usual tangential and normal body coordinates. In this report, the body-normal coordinates are used up to the first horizontal tangent; and beyond that point, a sheared cylindrical system is introduced. To derive equations in body-normal coordinates, Equation (1) is first written in a general curvilinear coordinate system as

$$\frac{a^2}{h_1 h_2 h_3} \left[\frac{\partial}{\partial x_1} (h_2 h_3 u) + \frac{\partial}{\partial x_2} (h_3 h_1 v) + \frac{\partial}{\partial x_3} (h_1 h_2 w) \right.$$

$$= \frac{1}{2} \left(\frac{u}{h_1} \frac{\partial}{\partial x_1} + \frac{v}{h_2} \frac{\partial}{\partial x_2} + \frac{w}{h_3} \frac{\partial}{\partial x_3} \right) |u\vec{i} + v\vec{j} + w\vec{k}|^2 \qquad (2)$$

where u, v, and w are the x_1, x_2, and x_3 components of the velocity vector $\vec{q}$; and h_1, h_2, and h_3 are the corresponding metrics.

3

For body-normal coordinates, the metrics are

$$h_1 = 1 + \kappa\eta \qquad (3a)$$

$$h_2 = 1 \qquad (3b)$$

$$h_3 = r + \eta \cos\theta \qquad (3c)$$

where θ and κ are the angle (measured counterclockwise from the axis of symmetry) and curvature of the reference coordinate surface; r is the radius from the axis; and the corresponding coordinates are

$$x_1 = \xi \qquad (4a)$$

$$x_2 = \eta \qquad (4b)$$

$$x_3 = \zeta \qquad (4c)$$

as depicted in Figure 1. Notice that w = 0 for axisymmetric cases. Now Equation (2) can be expressed as follows:

$$(a^2 - u^2)\frac{1}{H} u_\xi - uv(\frac{1}{H} v_\xi + u_\eta) + (a^2 - v^2)v_\eta$$

$$+ a^2(\frac{\kappa}{H} + \frac{\cos\theta}{r})v + a^2 \frac{\sin\theta}{r} u = 0 \qquad (5)$$

where $H = h_1 = 1 + \kappa\eta$, and subscripts denote partial differentiation. Define a velocity function ϕ and a rotation function F to relate velocity components u and v as follows:

$$u = \frac{1}{H} \phi_\xi + (1 + F)\cos\theta \qquad (6a)$$

$$v = \phi_\eta - (1 + F)\sin\theta \qquad (6b)$$

Then Equation (5) can be reduced to a second-order partial differential equation in ϕ with rotation function derivatives as forcing functions as follows:

$$(1 - \frac{u^2}{a^2})\frac{1}{H}(\frac{1}{H}\phi_\xi)_\xi - \frac{2uv}{a^2 H}\phi_{\xi\eta} + (1 - \frac{v^2}{a^2})\phi_{\eta\eta}$$

$$+ \ (\frac{2uv}{a^2} \frac{\kappa}{H} + \frac{\sin\theta}{r}) \ \frac{1}{H} \ \phi_\xi + [(1 - \frac{u^2}{a^2}) \ \frac{\kappa}{H} + \frac{\cos\theta}{r}] \phi_\eta$$

$$+ \ [\frac{uv}{a^2} \sin\theta + (1 - \frac{u^2}{a^2})\cos\theta] \ \frac{1}{H} \ F_\xi$$

$$- \ [\frac{uv}{a^2} \cos\theta + (1 - \frac{v^2}{a^2})\sin\theta]F_\eta = 0 \qquad\qquad (7)$$

This equation is similar to the corresponding uniform flow disturbance potential equation with the addition of rotation function derivatives as forcing functions.

In the sheared cylindrical coordinates, the velocity function ϕ and the rotation function F ar related to velocity components u, v, as

$$u = 1 + F + \phi_\xi - r_b' \phi_\eta \qquad\qquad (8a)$$

$$v = \phi_\eta \qquad\qquad (8b)$$

Thus the governing equation becomes

$$(1 - \frac{u^2}{a^2})\phi_{\xi\xi} - 2[r_b'(1 - \frac{u^2}{a^2}) + \frac{uv}{a^2}]\phi_{\xi\eta}$$

$$+ \ [(1 - \frac{v^2}{a^2}) + (r_b')^2(1 - \frac{u^2}{a^2}) + \frac{2uv}{a^2} r_b']\phi_{\eta\eta}$$

$$+ \ [\frac{1}{r} - r_b''(1 - \frac{u^2}{a^2})]\phi_\eta + (1 - \frac{u^2}{a^2})F_\xi$$

$$- \ [r_b'(1 - \frac{u^2}{a^2}) + \frac{uv}{a^2}]F_\eta = 0 \qquad\qquad (9)$$

where ξ is identified with the axial coordinate, x, and η is a transformed radial coordinate such that $\eta = 0$ is the body surface. The body shape enters Equation (9) through the first derivative

r_b' and the second derivative r_b'' of the local body radius, where primes mean differentiation with respect to x. With the two coordinate systems joined as described, the body surface is a coordinate surface where $\eta = 0$, and this simplifies the application of the surface flow tangency condition. It is also observed that Equation (9) has the same coefficients as the uniform-flow disturbance potential formulation again except the F_ξ and F_η terms.

2.2 Equation at the Axis

Along the axis of symmetry (the stagnation streamline) the limiting form of Equation (5) must be used to properly treat the terms involving $\frac{1}{r}$. The following symmetry conditions are used:

$$\phi_\xi = 0 \tag{10a}$$

$$F_\xi = 0 \tag{10b}$$

and since $\theta = 90°$ at the axis of symmetry,

$$u = 0. \tag{10c}$$

The following limits are used as $\xi \to 0$:

$$\frac{\cos\theta}{r} \to \frac{\kappa\sin\theta}{H\sin\theta} = \frac{\kappa}{H} \tag{11a}$$

$$\frac{u}{r} \to \frac{(\frac{1}{H}\phi_\xi)_\xi}{H\sin\theta} = \frac{1}{H}(\frac{1}{H}\phi_\xi)_\xi = \frac{1}{H^2}\phi_{\xi\xi} - \frac{\kappa}{H}\phi_\xi = \frac{1}{H_o^2}\phi_{\xi\xi} \tag{11b}$$

where the subscript o denotes a quantity on the axis. Since the rotation function is constant along the axis,

$$F_\eta = 0 \tag{12}$$

Hence at the axis, Equation (5) becomes

$$\frac{2}{H_o^2}\,\phi_{\xi\xi} + \left(1 - \frac{v_o^2}{a_o^2}\right)\phi_{o_{\eta\eta}} + 2\,\frac{\kappa_o}{H_o}\,\phi_{o\eta} = 0 \tag{13}$$

Notice that the rotation function derivatives are not present in Equation (13) and that Equation (13) is identical to the uniform-flow potential formulation.

2.3 Rotation Function

The vorticity vector $\vec{\omega}$ is defined as the curl of the velocity vector and can be shown to be

$$\vec{\omega} = \nabla \times \vec{q}$$

$$= \frac{1}{H}\,[v_\xi - (Hu)_\eta]\,\vec{k}$$

$$= -\left(\frac{\sin\theta}{H}\,F_\xi + F_\eta\cos\theta\right)\vec{k} \tag{14}$$

Its magnitude can be further linked to thermodynamic properties as (Ref. 2)

$$\frac{\sin\theta}{H}\,F_\xi + F_\eta\cos\theta = \frac{\gamma R}{u\left(1 + \frac{\gamma - 1}{2}M^2\right)}\left(\frac{M^2}{2}\,T_{o\eta} + \frac{T_o}{\gamma P_o}\,P_{o\eta}\right) \tag{15}$$

where $R = 1$ is the normalized gas constant, T is the temperature, P is the pressure, M is the local Mach number, γ is the ratio of specific heats, and the subscript o denotes stagnation quantities. Note that all variables in the above have been implicitly normalized with respect to the ambient velocity q_a and the ambient pressure P_a. Define the stream function ψ as follows:

$$\psi(\eta) = \int_o^\eta \rho u\,d\tau \tag{16}$$

where τ is a dummy variable and ρ is the local density.

Since stagnation quantities are constant along a streamline, the stream function ψ can be used to identify the stagnation pressure P_o, the stagnation density ρ_o, the stagnation temperature T_o, and thus the stagnation speed of sound a_o. After local Mach numbers are calculated, the local density can be obtained by the isentropic relation

$$\rho = \rho_o / (1 + \frac{\gamma - 1}{2} M^2)^{\frac{1}{\gamma - 1}} \tag{17}$$

In sheared cylindrical coordinates, the vorticity vector is

$$\vec{\omega} = (v_x - u_y)\vec{k} = -F_\eta \vec{k} \tag{18}$$

So Equation (15) becomes

$$F_\eta = \frac{\gamma R}{u(1 + \frac{\gamma - 1}{2} M^2)} (\frac{M^2}{2} \frac{\partial T_o}{\partial \eta} + \frac{T_o}{\gamma P_o} \frac{\partial P_o}{\partial \eta}) \tag{19}$$

Because Equation (19) is identical to Equation (15) if θ is equal to zero, the boundaries of these two coordinates are therefore chosen to be the first horizontal tangent on the body surface.

Now the solution procedures to calculate the rotation function can be stated as follows:

(1) For each constant ξ, assume the initial local density to be that of the undisturbed one.

(2) Calculate the stream function using Equation (16).

(3) Interpolate ρ_o, P_o, and T_o; and calculate a_o, M, and ρ, using Equation (17).

(4) Obtain $T_{o\eta}$ and $P_{o\eta}$ by applying cubic spline interpolation to $T_o(\eta)$ and $P_o(\eta)$ values.

(5) Repeat steps (2) - (4) until density converges.

(6) Integrate F_η to obtain the rotation function by moving F_ξ term
to the right side of Equation (15).

The iterative process will converge in several iterations.

2.4 Pressure Coefficients

Along a streamline, the following form of energy equation for a
perfect gas can be used:

$$\frac{1}{2} q^2 + \frac{a^2}{\gamma - 1} = \frac{1}{2} q_\infty^2(\psi) + \frac{a_\infty^2(\psi)}{\gamma - 1} = \frac{a_o^2(\psi)}{\gamma - 1} \qquad (20)$$

If the entropy is assumed to be nearly constant along a
streamline, i.e. only weak shocks are present, the pressure
coefficient can be derived from Equation (20) as

$$
\begin{aligned}
C_p &= \frac{P - P_\infty}{\frac{1}{2} \rho_{\infty_{ref}} q_{\infty_{ref}}^2} \\
&= \frac{2}{\gamma M_{\infty_{ref}}^2} \left\{ \left[1 + \frac{\gamma - 1}{2} M_\infty^2(\psi)(1 - \frac{|\vec{q}|^2}{|\vec{q}_\infty(\psi)|^2}) \right]^{\frac{\gamma}{\gamma-1}} - 1 \right\}
\end{aligned}
\qquad (21)
$$

2.5 Coordinate Stretching Functions

The normal coordinate η will be stretched according to the
following relation (Ref. 1),

$$\eta = \frac{Ay}{(1 - y)^\alpha} \qquad (22)$$

where y is the computational coordinate which varies from zero at the body to one at infinity. The constant A controls the physical step size at the body (denoted as o), $A = \eta_{y_o}$; and for a given value of A, the exponent α controls the size of the last finite value of η. Large values of α move points farther away from the body.

The tangential coordinate stretching to be used is a transformation between the physical arc length along the reference surface, ξ, and the computational coordinate, x, which varies from zero to one. For closed bodies the transformation is (Ref. 1)

$$\xi = \frac{\xi_{max}}{2} + (x - \frac{1}{2})[A + B(x - \frac{1}{2})^2] \qquad (23)$$

where A and B are determined by specifying ξ_{x_o} (o denotes nose or x = 0) and requiring that $\xi = \xi_{max}$ at x = 1. These conditions give

$$A = \frac{1}{2}(3\xi_{max} - \xi_{x_o}) \qquad (24a)$$

$$B = 4(\xi_{max} - A) \qquad (24b)$$

For open bodies the tangential coordinate stretching is divided into two regions with the physical location of the dividing point being x_m. The stretching function for the region from the nose up to x_m is given by (Ref. 1)

$$\xi = a_1 x + a_2 x^3 + a_3 x^5 + a_4 x^7 \qquad 0 \leqslant x \leqslant x_m \qquad (25)$$

In the region from x_m to infinity, the stretching function is (Ref. 1)

$$\xi = \xi_m + b \frac{(x - x_m)(1 - x_m)}{1 - x} \qquad x_m \leqslant x < 1 \qquad (26)$$

10

The coefficients in these expressions are determined by specifying ξ_m, ξ_{x_o}, and $\xi_{x_{xm}}$ and requiring that ξ_x and ξ_{xx} be continuous at $x = x_m$. These conditions give (Ref. 1)

$$a_1 = \xi_{x_o} \qquad\qquad b = \xi_{x_{xm}}$$

$$a_2 = \frac{70c_1 - 22c_2 + 2c_3}{16\,x_m^2}$$

$$a_3 = \frac{-84c_1 + 36c_2 - 4c_3}{16x_m^4}$$

$$a_4 = \frac{30c_1 - 14c_2 + 2c_3}{16x_m^6} \qquad\qquad (27)$$

where

$$c_1 = \frac{\xi_m - a_1 x_m}{x_m}$$

$$c_2 = b - a_1$$

and

$$c_3 = \frac{2x_m b}{1 - x_m}$$

Now, in the region of body normal coordinates, Equations (6a, b) and (7) become

$$u = \frac{f}{H}\,\phi_\xi + (1 + F)\cos\theta \qquad\qquad (28a)$$

$$v = g\phi_\eta - (1 + F)\sin\theta \qquad\qquad (28b)$$

$$(1 - \frac{u^2}{a^2}) \frac{f}{H} (\frac{f}{H} \phi_\xi)_\xi - \frac{2uvfg}{a^2 H} \phi_{\xi\eta} + (1 - \frac{v^2}{a^2})g(g\phi_\eta)_\eta$$

$$+ (\frac{2uv}{a^2} \frac{\kappa}{H} + \frac{\sin\theta}{r}) \frac{f}{H} \phi_\xi + [(1 - \frac{u^2}{a^2}) \frac{\kappa}{H} + \frac{\cos\theta}{r}]g\phi_\eta$$

$$+ [\frac{uv}{a^2} \sin\theta - (1 - \frac{u^2}{a^2})\cos\theta] \frac{f}{H} F_\xi$$

$$- [\frac{uv}{a^2} \cos\theta + (1 - \frac{v^2}{a^2})\sin\theta]gF_\eta = 0 \qquad (29)$$

Likewise in the region of sheared cylindrical coordinates, Equations (8a, b) and (9) are transformed into the following:

$$u = 1 + F + f\phi_\xi - r_b' g\phi_\eta \qquad (30a)$$

$$v = g\phi_\eta \qquad (30b)$$

and

$$(1 - \frac{u^2}{a^2})f(f\phi_\xi)_\xi - 2fg[r_b'(1 - \frac{u^2}{a^2}) + \frac{uv}{a^2}]\phi_{\xi\eta}$$

$$+ [(1 - \frac{v^2}{a^2}) + (r_b')^2(1 - \frac{u^2}{a^2}) + \frac{2uv}{a^2} r_b']g(g\phi_\eta)_\eta$$

$$+ [\frac{1}{r} - r_b''(1 - \frac{u^2}{a^2})]g\phi_\eta + (1 - \frac{u^2}{a^2})fF_\xi$$

$$- [r_b'(1 - \frac{u^2}{a^2}) + \frac{uv}{a^2}]gF_\eta = 0 \qquad (31)$$

If $r_b' = 0$ and $r_b'' = 0$ in the region of body normal coordinates and $\theta = 0$ and $\kappa = 0$ in the region of sheared cylindrical coordinates, Equations (28a,b), (29), (30a, b) and (31) can be combined into a single set of equations.

$$u = \frac{f}{H} \phi_\xi + (1 + F)\cos\theta - r_b'g\phi_\eta \tag{32a}$$

$$v = g\phi_\eta - (1 + F)\sin\theta \tag{32b}$$

and

$$(1 - \frac{u^2}{a^2}) \frac{f}{H} (\frac{f}{H} \phi_\xi)_\xi - 2[r_b'(1 - \frac{u^2}{a^2}) + \frac{uv}{a^2}]fg\phi_{\xi\eta}$$

$$+ [(1 - \frac{v^2}{a^2}) + (r_b')^2(1 - \frac{u^2}{a^2}) + \frac{2uv}{a^2} r_b']g(g\phi_\eta)_\eta$$

$$+ (\frac{2uv}{a^2} \frac{\kappa}{H} + \frac{\sin\theta}{r}) \frac{f}{H} \phi_\xi + [(1 - \frac{u^2}{a^2}) \frac{\kappa}{H} + \frac{\cos\theta}{r}$$

$$- r_b''(1 - \frac{u^2}{a^2})]g\phi_\eta + [\frac{uv}{a^2} \sin\theta + (1 - \frac{u^2}{a^2})\cos\theta] \frac{f}{H} F_\xi$$

$$- [\frac{uv}{a^2} \cos\theta + (1 - \frac{v^2}{a^2})\sin\theta + r_b'(1 - \frac{u^2}{a^2})]gF_\eta = 0 \tag{33}$$

2.6 Rotated Finite Difference Scheme

Rotated difference (Ref. 12) is needed to keep diagonal dominance of the tridiagonal implicit scheme and the correct zone of dependence and thus the numerical stability. In the case of body normal coordinates, Equation (28a, b) and (29), the streamwise and normal derivatives ϕ_{SS} and ϕ_{NN} are given by

$$\phi_{SS} = \frac{1}{q^2} [\frac{u^2}{H} (\frac{1}{H} \phi_\xi)_\xi + \frac{2uv}{H} \phi_{\xi\eta} + v^2\phi_{\eta\eta}] \tag{34a}$$

$$\phi_{NN} = \frac{1}{q^2} [\frac{v^2}{H} (\frac{1}{H} \phi_\xi)_\xi - \frac{2uv}{H} \phi_{\xi\eta} + u^2\phi_{\eta\eta}] \tag{34b}$$

13

where S and N are the streamwise and normal directions to a streamline.

In the sheared cylindrical coordinates, Equations (30a, b) and (31), ϕ_{SS} and ϕ_{NN} are given as

$$\phi_{SS} = \frac{1}{q^2} [u^2 \phi_{\xi\xi} + 2u(v - r_b'u)\phi_{\xi\eta} + (v - r_b'u)^2 \phi_{\eta\eta}] \qquad (35a)$$

$$\phi_{NN} = \frac{1}{q^2} [v^2 \phi_{\xi\xi} - 2v(u + r_b'v)\phi_{\xi\eta} + (u + r_b'v)^2 \phi_{\eta\eta}] \qquad (35b)$$

Now Equation (33) is written in the form:

$$(1 - \frac{q^2}{a^2})\phi_{SS} + \phi_{NN} + (\frac{2uv}{a^2} \frac{\kappa}{H} + \frac{\sin\theta}{r}) \frac{f}{H} \phi_{\xi}$$

$$+ [(1 - \frac{u^2}{a^2}) \frac{\kappa}{H} + \frac{\cos\theta}{r} - r_b''(1 - \frac{u^2}{a^2})]g\phi_{\eta}$$

$$+ [\frac{uv}{a^2} \sin\theta + (1 - \frac{u^2}{a^2})\cos\theta] \frac{f}{H} F_{\xi}$$

$$- [\frac{uv}{a^2} \cos\theta + (1 - \frac{v^2}{a^2})\sin\theta + r_b'(1 - \frac{u^2}{a^2})]gF_{\eta} = 0 \qquad (36)$$

At supersonic points, upwind differences are used for the three second derivatives contributing to ϕ_{SS}, and central differences are used for those contributing to ϕ_{NN} and all first derivatives. At subsonic points, the usual procedure is used with central differences for all derivatives directly in Equation (33). Thus at subsonic points the truncation error is formally of the second order, while at supersonic points it is of the first order.

Equation (36) is seen to be quite similar to that used in RAXBOD (Ref. 12), except for the rotation function derivatives. Therefore, Keller and South's transonic disturbance potential code, RAXBOD, is modified to solve the present problem.

2.7 Boundary Conditions

At infinity, the perturbation potential is required to vanish; that is,

$$\phi \to 0 \text{ as } \eta \to \infty \tag{37}$$

In sheared cylindrical coordinates, the perturbations at downstream infinity ($\xi \to \infty$) must likewise vanish. This can be accomplished via transformation $\tau = \tau(\xi)$ by mapping $\xi = \infty$ to a finite value of τ, or one can simply use a sufficiently large ξ and apply $\phi = 0$ there, or extrapolate ϕ when $M(r)_{inf} > 1$. The latter course was taken in the present study. That is, for $M(r)_{inf} < 1$, the downstream boundary is located about three-fourths to one body length beyond the sting/body junction or other most downstream obstacle. For $M(r)_{inf} > 1$, the only requirement is that the boundary must be downstream of the last subsonic region. Numerical results are otherwise insensitive to the precise location of the boundary.

On the surface, $\eta = 0$, the flow tangency condition depends on the coordinate system as follows:

Body Coordinates:

$$v = 0 \tag{38a}$$

or

$$\phi_\eta = (1 + F)\sin\theta \tag{38b}$$

Sheared Cylindrical Coordinates:

$$v - ur_b' = 0 \tag{39a}$$

or

$$\phi_\eta = \frac{r_b'}{1 + (r_b')^2} (1 + F + \phi_\xi) \tag{39b}$$

In the sheared cylindrical coordinates, the body surface
boundary condition is satisfied by introducing dummy points inside
the body. Details can be found in Reference 1. For completeness,
the formulation is described in the following. Note that the dummy
points may be located above or below the symmetry axis. For dummy
points above the axis, as shown in Figure 2(a), the values of the
potential function at these dummy points are computed through
Equation (39b).

$$\phi_y = \frac{\phi_{i, jmax-1} - \phi_{i, jmax+1}}{2\Delta y} \, ,$$

or

$$\phi_{i, jmax+1} = \phi_{i, jmax-1} - \phi_y/2\Delta y \tag{40}$$

Note that $\phi_\eta = \phi_y y_\eta$ through Equation (22). It is possible that
dummy points may be below the axis, as shown in Figures (2b) and
(2c). Due to symmetry, the potential at a point below the axis
should be the same as that for a point (i.e., the image point) at an
equal distance above the axis. In this case, let y_1 be the
computational coordinate at the image dummy point where the
potential is to be calculated. A Taylor series expansion for ϕ at
this point (which is the same as $\phi_{i, jmax+1}$) yields (Ref. 1)

$$\phi_{i, jmax+1} = \phi_{i, jmax} + y_1\phi_y + \frac{y_1^2}{2} \phi_{yy} + \cdot \cdot \cdot \tag{41a}$$

16

Similarly,

$$\phi_{i,jmax-1} = \phi_{i,jmax} + \Delta y \phi_y + \frac{\Delta y^2}{2} \phi_{yy} + \cdots \qquad (41b)$$

Eliminating ϕ_{yy} from these equations and solving for $\phi_{i,jmax+1}$, it is obtained that

$$\phi_{i,jmax+1} = \frac{y_1^2}{(\Delta y)^2} \phi_{i,jmax-1} + (1 - \frac{y_1^2}{(\Delta y)^2})\phi_{i,jmax} + y_1(1 - \frac{y_1}{\Delta y})\phi_y$$

$$(42)$$

To calculate y_1, the computational coordinate corresponding to the location of the axis, y_a, is first obtained. Then $y_1 = \Delta y + 2y_a$. Note that y_a is negative. y_a can be found from the stretching function (Equation 22) by expansion in a series for a small y to give

$$\frac{\eta}{A} = y + \alpha y^2 + \frac{\alpha(\alpha + 1)}{2} y^3 + \frac{\alpha(\alpha + 1)(\alpha + 2)}{6} y^4 + \cdots \qquad (43)$$

Equation (43) can be inverted to give

$$y = \frac{\eta}{A} - \alpha(\frac{\eta}{A})^2 + \frac{\alpha(3\alpha - 1)}{2} (\frac{\eta}{A})^3 - \frac{\alpha(16\alpha^2 - 12\alpha + 2)}{6} (\frac{\eta}{A})^4 + \cdots$$

$$(44)$$

Putting $\eta = -r_b$ into Equation (44) gives the value of y_a.

2.8 Grid Halving

A considerable saving in computing time can be achieved by first obtaining the solution on a coarse grid and then halving the mesh size in both directions for further calculation. This process can be continued to any desired mesh refinement within the computer time and storage limitations. The following third-order

17

interpolation formulas are used to interpolate results in a coarser

grid to those in a finer grid:

1) For points next to symmetry axis,

$$\phi_{i,j} = .5625\phi_{i-1,j} + .5\phi_{i+1,j} - .0625\phi_{i+3,j} \tag{45a}$$

if the symmetry axis is at i − 1;

$$\phi_{i,j} = .5625\phi_{i+1,j} + .5\phi_{i-1,j} - .0625\phi_{i-3,j} \tag{45b}$$

if the symmetry axis is at i + 1.

2) For points not next to symmetry axis,

$$\phi_{i,j} = .3125\phi_{i-1,j} + .9375\phi_{i+1,j} - .3125\phi_{i+3,j}$$
$$+ .0625\phi_{i+5,j} \tag{46a}$$

if the symmetry axis is at i − 1;

$$\phi_{i,j} = .3125\phi_{i+1,j} + .9375\phi_{i-1,j} - .3125\phi_{i-3,j}$$
$$+ .0625\phi_{i-5,j} \tag{46b}$$

if the symmetry axis is at i + 1.

Similar formulas are also used in the j direction.

2.9 Optimization formulation:

CONMIN (Ref. 13) is used to couple the present program for

designing an axisymmetric body.

The objective function OBJ is formulated as

$$OBJ = -0.1/(0.001 + C_{d_w}) \tag{47}$$

where C_{d_w} is the pressure drag.

The maximum thickness is assumed to be constrained. It is formulated as

$$G(1) = 10\left(\frac{r_{max}}{r_{upper}} - 1\right) \qquad (48a)$$

$$G(2) = 10\left(1 - \frac{r_{max}}{r_{lower}}\right) \qquad (48b)$$

where r_{max} is the maximum radius. G is the constraint function. Since equality constraints are not practical numerically for nonlinear problems, an upper limit r_{upper} and a lower limit r_{lower} are used instead. The constant, 10, is used to increase the relative importance of constraint gradients in finding the optimal direction during optimization.

The trailing-edge thickness can also be constrained. The constraint functions are defined as

$$G(3) = \frac{r_{te}}{t_{upper}} - 1 \qquad (49a)$$

$$G(4) = 1 - \frac{r_{te}}{t_{lower}} \qquad (49b)$$

if the constrained thickness, t, is not zero. Otherwise, they are

$$G(3) = 100(r_{te} - t_{upper}) \qquad (50a)$$

$$G(4) = 100(t_{lower} - r_{te}) \qquad (50b)$$

Since transonic computation is very CPU-intensive, the following representation of body shapes is used to reduce the number of design variables. For an ellipsoid-type body, the slope of the

19

body shape is expressed in a series as follows:

$$\frac{dr}{dx} = \frac{A_{n+1}}{2} \cot \frac{\theta}{2} - \frac{A_{n+2}}{2} \tan \frac{\theta}{2} + \sum_{1}^{N} A_n \sin n\theta \qquad (51a)$$

$$x = x_i + \frac{x_\ell - x_i}{2} (1 - \cos\theta) \qquad (51b)$$

where $\cot \frac{\theta}{2}$ and $\tan \frac{\theta}{2}$ take care of the leading edge and trailing edge slopes, respectively; x_i is the starting x coordinate; x_ℓ is the ending x coordinate; θ is the corresponding angle in the transformed plane; and N is the number of coefficients in the sine series. The body shape can be integrated to give

$$r = \int \frac{dr}{dx} dr$$

$$= \frac{\ell}{2} \{ \frac{A_{N+1}}{2} (\theta + \sin\theta) - \frac{A_{N+2}}{2} (\theta - \sin\theta) + \frac{A_1}{2} (\theta - \frac{\sin 2\theta}{2})$$

$$+ \sum_{n=2}^{N} A_n [\frac{\sin(n-1)\theta}{n-1} - \frac{\sin(n+1)\theta}{n+1}] \} \qquad (52)$$

By defining the following quantities

$$\theta = \cos^{-1}(\frac{2x}{\ell} - 1)$$

$$x_\mu = \frac{\ell}{2} (1 + \cos \frac{\mu\pi}{M}), \text{ M even, } 1 < \mu < M - 1$$

Weber (Ref. 14) showed that the leading edge radius $r_{\ell e}$ is given by

$$\sqrt{2 \frac{r_{\ell e}}{\ell}} = -2 \sum_{\mu=1}^{M-1} (-1)^\mu \frac{\sin\phi_\mu}{1 + \cos\phi_\mu} \frac{r_\mu}{\ell} \qquad (53)$$

$$A_{N+1} = \sqrt{2 \frac{r_{\ell e}}{\ell}} = -2 \sum_{\mu=1}^{M-1} (-1)^\mu \frac{\sin\phi_\mu}{1 + \cos\phi_\mu} \frac{r_\mu}{\ell} \qquad (54)$$

$$A_{N+2} = \sqrt{2 \frac{r_{te}}{\ell}} = -2 \sum_{\mu=1}^{M-1} (-1)^\mu \frac{\sin\phi_\mu}{1 - \cos\phi_\mu} \frac{r_\mu}{\ell} \qquad (55)$$

20

and

$$A_1 = \frac{4r_{te}}{\pi \ell} - A_{N+1} + A_{N+2} \tag{56}$$

Let $f(\theta) = \frac{2r}{\ell} - \frac{A_{N+1}}{2}(\theta + \sin\theta) + \frac{A_{N+2}}{2}(\theta - \sin\theta)$

$$- \frac{A_1}{2}(\theta - \frac{\sin 2\theta}{2})$$

$$= \sum_{2}^{N} A_n [\frac{\sin(n-1)\theta}{n-1} - \frac{\sin(n+1)\theta}{n+1}] \tag{57}$$

Multiply (57) by

$$\frac{\sin(m-1)\theta}{m-1} - \frac{\sin(m+1)\theta}{m+1}$$

and integrate with respect to θ to obtain

$$\int_{o}^{\pi} f(\theta)[\frac{\sin(m-1)\theta}{m-1} - \frac{\sin(m+1)\theta}{m+1}]d\theta$$

$$= \frac{\pi}{2}\{\frac{A_m - A_{m-2}}{(m-1)^2} + \frac{A_m - A_{m+2}}{(m+1)^2}\}$$

$$= \frac{\pi}{2}\{A_m[\frac{1}{(m-1)^2} + \frac{1}{(m+1)^2}]$$

$$- \frac{A_{m-2}}{(m-1)^2} - \frac{A_{m+2}}{(m+1)^2}\} \tag{58}$$

Therefore,

$$A_m[\frac{1}{(m-1)^2} + \frac{1}{(m+1)^2}] = \frac{A_{m-2}}{(m-1)^2} + \frac{A_{m+2}}{(m+1)^2}$$

$$+ \frac{2}{M}\sum_{k=1}^{M} f(\theta_k)[\frac{\sin(m-1)\theta_k}{m-1} - \frac{\sin(m+1)\theta_k}{m+1}], \quad m > 2 \tag{59}$$

Note that r_{te} may become negative during the optimization process. In this case, the coefficient A_{N+2} is slightly reduced repeatedly until r_{te} is nonnegative.

To find r_{max}, $dr/d\theta$ is set to zero:

$$\frac{dr}{d\theta} = \frac{\ell}{2} \left\{ \frac{A_{N+1}}{2} (1 + \cos\theta) - \frac{A_{N+2}}{2} (1 - \cos\theta) + \frac{A_1}{2} (1 - \cos 2\theta) \right.$$

$$\left. + \sum_2^N A_n [\cos(n-1)\theta - \cos(n+1)\theta] \right\}$$

$$= \frac{\ell}{2} \left\{ \frac{A_{N+1}}{2} (1 + \cos\theta) - \frac{A_{N+2}}{2} (1 - \cos\theta) + \frac{A_1}{2} (1 - \cos 2\theta) \right.$$

$$\left. + 2 \sum_2^N A_n \sin n\theta \sin\theta \right\}$$

$$= 0 \qquad\qquad (60)$$

Let

$$I(\theta) = \frac{A_{N+1}}{2} (1 + \cos\theta) - \frac{A_{N+2}}{2} (1 - \cos\theta) + \frac{A_1}{2} (1 - \cos 2\theta)$$

$$+ 2 \sum_2^N A_n \sin n\theta \sin\theta \qquad\qquad (61)$$

Then

$$I'(\theta) = - \frac{A_{N+1}}{2} \sin\theta - \frac{A_{N+2}}{2} \sin\theta + A_1 \sin 2\theta$$

$$+ 2 \sum_2^N A_n [n \cos n\theta \sin\theta + \sin n\theta \cos\theta] \qquad\qquad (62)$$

θ at r_{max} can be iteratively solved by Newton's method as

$$I(\theta) + I'(\theta_i)(\theta_{i+1} - \theta_i) = 0 \ ,$$

or

$$\theta_{i+1} = \theta_i - \frac{I(\theta_i)}{I'(\theta_i)} \qquad\qquad (63)$$

For a body with nonblunt trailing edge, the shape function given by Equation (52) is found inappropriate because the coefficient A_{N+1} is too dominating. Any change in A_{N+1} will affect

22

not only the nose shape but also the trailing-edge thickness quite significantly. Therefore, the shape function is redefined to be

$$r = \frac{\ell}{2} \left\{ A_{N+1} \sin\theta \cos\frac{\theta}{2} + \sum_{n=1}^{N} A_n \cos(n-1)\theta \right\} \tag{64}$$

It can be shown that A_{N+1} is still related to the leading-edge radius through Equation (54). A_n, $n < N$, are determined as Fourier coefficients in the usual manner.

3. NUMERICAL RESULTS AND DISCUSSIONS

Examination of the governing equation (Equation 9) for the present nonuniform flow problem indicates that the equation is similar to that for the uniform flow except the "nonhomogeneous" F-terms. Therefore, it is appropriate and convenient to modify the uniform-flow code of Reference 1 to solve the present problem.

Before numerical results are presented, first some considerations of numerical stability and convergence of the revised code will be given. Relaxation and supersonic damping factors, as discussed in Reference 12, are needed to ensure stability and convergence. Therefore, they will be considered next.

3.1 Numerical Stability

Stability is indicated by $\Delta\phi_{max}$. Since the governing equation involves a $\frac{1}{r}$-term, $\Delta\phi_{max}$ occurs usually on the symmetry axis or on the body surface. With the addition of F_ξ and F_η terms, the location of $\Delta\phi_{max}$ moves to where the maximum values of these terms occur. The latter are somewhere ahead of the nose and away from the axis. When shock is strong, the solution and $\Delta\phi_{max}$ may be oscillatory.

3.2 Convergence

Residual of the governing equation is indicative of how well the current values of ϕ satisfy the governing equation and thus is

24

used as the convergence criterion of the present method. In subsonic or low transonic free stream, the value of the residual can be reduced to an arbitrarily small value. However, because of the first-order accuracy inherent at the supersonic points, this seldom can be done in high transonic or supersonic freestream. The location of maximum residual usually occurs at either the trailing edge or the nose stagnation point.

3.3 Relaxation and Supersonic Damping Factors

A relaxation factor is used to control the stability and convergence at subsonic points, while a supersonic damping factor is to increase the stability at supersonic points. When the sum of residuals of the last ten iterations increases, the original code will increase the value of the supersonic damping factor by 0.1 or decrease the relaxation factor by ten percent. It turns out in most cases that the maximum residual occurs at either the nose or the tail where the flow is usually subsonic. Therefore, the supersonic damping factor will not change during the iteration. Since $\Delta\phi_{max}$ is also an important indicator for stability and convergence and its location is usually not at the body surface, another indicator is set up to indicate whether the point with $\Delta\phi_{max}$ is subsonic or supersonic. Therefore, for each ten iterations, if either the $\Delta\phi_{max}$-point or the point of maximum residual is supersonic, the supersonic damping factor is increased by 0.1. Likewise, when either point is subsonic, the relaxation factor is decreased by ten

25

percent. The maximum supersonic damping factor is set to 3.0 and the minimum relaxation factor is set to 0.3. If for a continuous one hundred iterations the sum of maximum residual decreases, the supersonic damping factor is decreased by 0.1 when at either locations of maximum residual or $\Delta\phi_{max}$ the flow is supersonic. The relaxation factor is increased by ten percent when at either locations of maximum residual or $\Delta\phi_{max}$ the flow is subsonic. The minimum of supersonic damping is set to zero, while the maximum relaxation factor is an input quantity.

3.4 Numerical Results in Analysis

Experimental data for a body in axisymmetric nonuniform transonic flow are not available for comparison. Therefore, in the following only theoretical results will be presented to show the general trend. In uniform flow, some results with data comparison can be found in Reference 12.

The main motivation of this research is to find the nonuniformity effects on a propfan nacelle. The experimental Mach number profile of a propfan is plotted in Figure 3 with a scaled ellipsoid. Calculated pressure distributions shown in Figure 4 indicate that the pressure distribution in a nonuniform flow is more negative than that in a uniform flow with a Mach number equal to that either of the external flow or in the slipstream. Similar results have been obtained for a Joukowsky airfoil in two-dimensional incompressible flow in Reference 16. For an ellipsoid

26

with sting as shown in Figure 5, a similar trend in pressure

distribution as presented in Figure 6 is observed. Physically, it

is possible that this is due to the constraint effect of the outer

subsonic freestream which reflects the disturbance back to the

central region. The effect of sting on the ellipsoid is similar to

having a thick wake and is to decrease the pressure as shown in

Figure 7. Notice that in all cases shown above, no local supersonic

regions are present for the configuration used with a fineness ratio

of 10.

In Reference 8, Mach numbers of 0.98 and 1.1 were used in

determining axisymmetric bodies with minimum pressure drag in

uniform flow. Therefore, nonuniform transonic freestreams from Mach

0.98 to 1.1, 1.2, 1.3, and 1.4 are chosen in the present parametric

investigation. The following Mach profiles will be used (see

Figures 8a,b):

$$M_{inf}(r) = 1.4 - 0.42 \tanh(\frac{r}{d}) \tag{62}$$

where r is the radial distance and d controls the extent of the

nonuniformity region. As shown in Figure 9, it is seen that for the

same maximum Mach difference, the pressure distribution appears to

be about the same, irrespective of difference in profile shapes.

Note that C_p in Figure 9 and all that follow is based on the dynamic

pressure in the external uniform flow. This result is unexpected

because in References 15 and 16 the extent of nonuniformity was

shown to affect the pressure distribution of an airfoil in two-

dimensional flow. To investigate this problem further, step-type

27

nonuniform profiles shown in Figure 10 are employed. Again, the same results are obtained as shown in Figure 11.

On the other hand, for the configuration with sting in the same Mach profiles (Figure 12), some differences (Figure 13) do show up. However, for the step-type nonuniform profiles (Figure 14), all pressure distributions, again, are the same (Figure 15). In Figure 16, the sting effect is seen to reduce the shock peak. It also shows that the nonuniform Mach profile shape is not an important parameters in the present problem. One possible reason for this is that there is no vortex flow in the present axisymmetric cases, i.e. with zero lift, while in the airfoil problem (Refs. 15 and 16), lift is significant.

Since the nonuniform Mach profile shape is not an important parameter in the present study, nonuniform extent of d = 0.1 will be used in the following to investigate the effect of nonuniformity magnitude. As shown in Figure 17, in supersonic nonuniform freestreams the magnitude of nonuniformity increases the pressure coefficient negatively and nonlinearly for the ellipsoid configuration. Similar trend can be seen for the ellipsoid/sting configuration. In a transonic nonuniform freestream, increasing the Mach number in the nonuniform region tends to make C_p more negative and move the shock rearward as shown in Figures 19 and 20. In Figure 21 it can be observed that the pressure is more negative in a subsonic outer stream and that the sting reduces the shock peaks.

In Figure 22, the drag coefficient is plotted for all cases investigated. It is seen that it is slightly negative for near-sonic nonuniform cases. This is because of the neglect of viscous drag and base drag. Transonic freestream is found to induce lower drag for near-sonic cases but higher drag for stronger nonuniformities. This is because at near sonic conditions transonic freestream wave drag is minimal. However with higher Mach numbers in the nonuniform region, the wave drag approaches that of a uniform supersonic freestream.

3.5 Numerical Results in Design Optimization

Chan's (Ref. 8) numerical results were obtained at Mach 0.98 and 1.1 in uniform flow. However, the starting shape to be used in the present investigation has been verified experimentally (Ref. 17) and numerically (Ref. 12) not to induce a shock wave until M = 0.986. Therefore, it is decided to use Mach 0.995 and 1.1 as typical Mach numbers for uniform subsonic and supersonic cases, respectively, and a nonuniform freestream varying from a Mach number of 0.995 to 1.1 for the nonuniform flow case. To reduce the number of design variables, representation of the body shape in a Fourier series as discussed in Section 2.9 is used. The number of design variables (i.e. the Fourier coefficients) can be reduced to six without sacrificing the accuracy. Since in transonic computation it takes too many iterations to converge when a variable is perturbed, the step size can not be too large. However, if a small step size

29

is used, the gradient of the objective function would be small so that the objective function will change little. Therefore, a user's judgment is needed in the design process. The following results are obtained after many cycles of optimization. In each cycle, only one to three iterations in CONMIN are used. The results may not represent the final optimum.

Ellipsoid

For the uniform supersonic case of Mach 1.1, the original and the final pressure distributions are compared in Figure 23. The original shape produces a gradual expansion until a tail shock is encountered. The designed shape results in a wavy pressure distribution ending with sudden expansion and shock at the tail. A drag reduction of 14 percent is achieved. The shapes are compared in Figure 24.. The designed shape shows a two-percent reduction in maximum thickness, with thickness reduced in the front, and the contour straightened in the rear.

For uniform subsonic freestream of Mach 0.995, a drag reduction of 5% and a minor pressure change, caused by reduction in shock strength, are seen in Figure 25. The designed shape shows slight thinning in the front and slight thickening in the rear, as shown in Figure 26.

For the case with nonuniform transonic freestream, it is observed in Figure 27 that the design pressure distribution eliminates the double shocks associated with the original shape. This results in a 13% reduction of drag and 1.18% increase of

maximum thickness. In Figure 28, the designed shape is shown to be slightly thinner in the front, thicker in the middle, and flatter in the rear.

In all cases, the location of maximum thickness stays the same in the subsonic case and shifts slightly forward in supersonic and transonic cases. Note that the original shape is shockless until M = 0.986. All cases considered here involve higher Mach numbers. It appears that by thinning the front and thickening the rear (to reduce the surface slope), the pressure drag can be reduced at the higher Mach numbers.

Body with NACA 0012-Type Contour

To design a body with a rounded leading edge and a trailing edge which is not blunt, an initial shape given by the NACA-0012 airfoil contour is chosen. Again, six design variables (A_n in Equation 64) are used. The maximum thickness is constrained to be between 13% and 11.5% and the trailing-edge thickness between 0% and 1%. As indicated in Reference 11, reducing the residual of the governing equation to a small value may not be needed for a reasonably accurate solution. Therefore, in the following design process, the convergence criterion is based on the maximum equation residual obtained in the analysis of the input shape. The final designed shape is then subject to further analysis through 1200 iterations for final plotting.

In a uniform flow with M = 0.98, the results are presented in Figures 29 and 30. As can be seen in Figure 29, the shape of the

NACA 0012 contour produces higher negative pressure behind the nose and a stronger shock which is more forward. By decreasing the nose radius and increasing the thickness in the aft portion (Figure 30), the designed shape produces less expansion to reduce the negative pressure level behind the nose and a weaker shock which is more aft. The achieved pressure drag reduction is about 46% with $\Delta c_d =$ 0.0187.

The same initial shape is again used in a nonuniform transonic flow. The Mach number in the external stream is 0.98. However, over an extent of nonuniform flow region equal to one-half of the body length, M is set to 0.995 around the body. Similar results in pressure distributions and change in body shape are obtained, as shown in Figures 31 and 32. That is, reducing the nose radius and increasing the thickness in the aft portion tend to reduce the wave drag. However, the pressure drag reduction is less than that in the uniform flow case, being 29% with $\Delta c_d = 0.0137$.

4. CONCLUSIONS

An inviscid nonuniform transonic axisymmetric body code capable
of performing analysis and design was developed. Numerical stabil-
ity and convergence behaviors were discussed, and so were the super-
sonic damping and relaxation factors. Numerical results showed that
nonuniformity caused pressure coefficient to be more negative.
Sting attached to the body was to reduce the pressure peak near the
juncture. If a shock was present, the strength was reduced and its
location moved forward. The extent and shape of the nonuniformity
region appeared to have little effect on pressure distribution.
Increase in nonuniformity magnitude would make C_p more negative and
the shock location more rearward.

The CONMIN optimizer was coupled with the present analysis code
to design axisymmetric bodies in uniform and nonuniform flow. For
an ellipsoid, the trend indicated that by thinning the front portion
and flattening the rear of a body, the pressure drag could be re-
duced at high transonic and low supersonic speeds. The drag reduc-
tion in a uniform flow of M = 1.1 and 0.995 was 14 percent and 5
percent, respectively. In a nonuniform flow of M = 0.995 to 1.1,
the pressure drag reduction achieved was 13 percent. For a body
with a rounded leading edge and nonblunt trailing edge, the nose
radius should be reduced and the thickness in the aft portion
slightly increased to decrease the pressure drag. Using the NACA
0012 contour as the initial shape, it was shown that a drag reduc-
tion of 46 percent and 29 percent was achieved, respectively, in a
uniform flow of M = 0.98 and a nonuniform flow of M = 0.98 to 0.995.

5. REFERENCES

1. Keller, J. D., and South, J. C., "RAXBOD: A Fortran Program for Inviscid Transonic Flow Over Axisymmetric Bodies." NASA TM-X-72831, February 1976.

2. Brown, E. F., Brecht, T. J. F., and Walsh, K. E., " A Relaxation Solution of Transonic Nozzle Flow Including Rotational Flow Effects." Journal of Aircraft, Vol. 14, No. 10, October 1977, pp. 944-951.

3. Chang, J.-F., and Lan, C. E., "Transonic Airfoil Analysis and Design in Nonuniform Flow." NASA CR-3991, June 1986.

4. Whitcomb, R. T., "Advanced Transonic Aerodynamic Technology." Advances in Engineering Science, Vol. 4, NASA CP-2001, November 1976, pp. 1521-1537.

5. Von Karman, T., "The Problems of Resistance in Compressible Fluids." Proceedings of the Fifth Volta Congress, R. Accad. d'Italia, 1936, pp. 222-283.

6. Sears, W. R., "On Projectiles of Minimum Wave Drag." Quarterly of Applied Mathematics, Vol. 14, 1947, pp. 361-366.

7. Haack, W., "Geschossformen Kleinsten Wellenwiderstandes." Lilienthal Geseilschaft, Bericht 139, 1941, pp. 14-28.

8. Chan, Y. Y., Mundle, D. L., and Jones, D. J., "Transonic Axisymmetric Bodies with Minimal Wave Drag." Canadian Aeronautics and Space Journal, Vol. 26, No. 3, Third Quarter 1980, pp. 231-234.

9. Chan, Y. Y., and Seager, S. M., "Computation of Transonic Flow Past Slender Bodies of Revolution." Laboratory Technical Report, LTR-HA-42, National Aeronautical Establishment, August 1979.

10. Kowalik, J., and Osborne, M. R., "Methods for Unconstrained Optimization Problems." Chapter 2, American Elsevier Publishing Co., Inc., New York, 1968.

11. South, J. C., Jr., and Jameson, A., "Relaxation Solution for Inviscid Axisymmetric Transonic Flow Over Blunt or Pointed Bodies." AIAA Computational Fluid Dynamics Conference, Palm Springs, Calif., July 1973, pp. 8-17.

12. Jameson, A., "Iterative Solution of Transonic Flow Over Airfoils and Wings, Including Flows at Mach 1." Communication of Pure and Applied Mathematics, Vol. 27, 1974, pp. 183-309.

13. Vanderplaats, G. N., "CONMIN—A Fortran Program for Constrained Function Optimization." NASA TM X-62282, August 1973.

14. Weber, J., "The Calculation of the Pressure Distribution Over the Surface of Two-Dimensional and Swept Wings With Symmetrical Airfoil Sections." British Aeronautical Research Council Reports and Memoranda, No. 2918, 1956.

15. Chow, F., Krause, E., Liu, C. H., and Mao, J., "Numerical Investigations of an Airfoil in a Nonunifrom Stream." Journal of Aircraft, Vol. 7, No. 6, Nov.-Dec. 1970, pp. 531-537.

16. Lan, C. E., "Wing-Slipstream Interaction with Mach Number Nonuniformity." Journal of Aircraft, Vol. 12, No. 10, October 1975, pp. 759-760.

17. Couch, L. M., and Brooks, C. W., Jr., "Effect of Blockage Ratio on Drag and Pressure Distributions for Bodies of Revolution at Transonic Speeds." NASA TN D-7331, 1973.
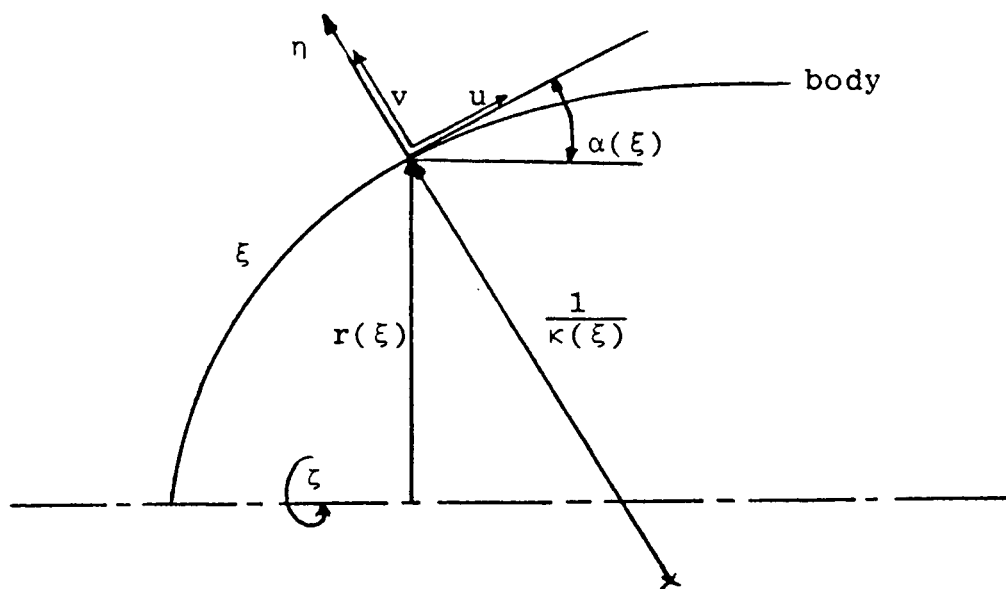
Figure 1. Axisymmetric Body Normal Coordinate
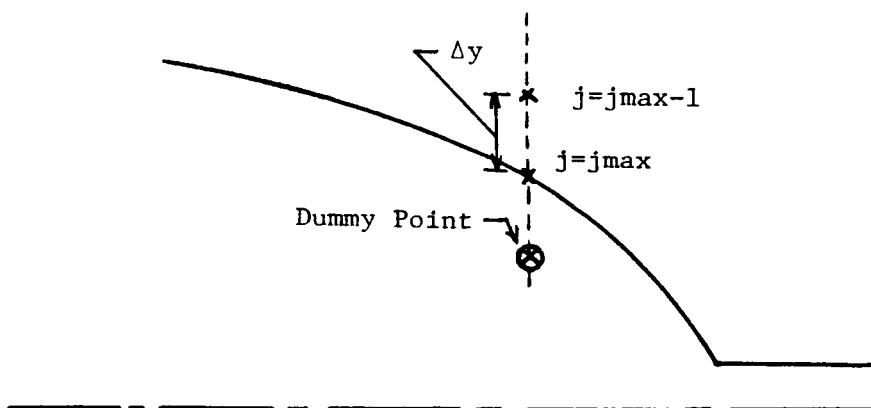
Figure 2a. Ordinary Dummy Point

image dummy point $\to$ y_a
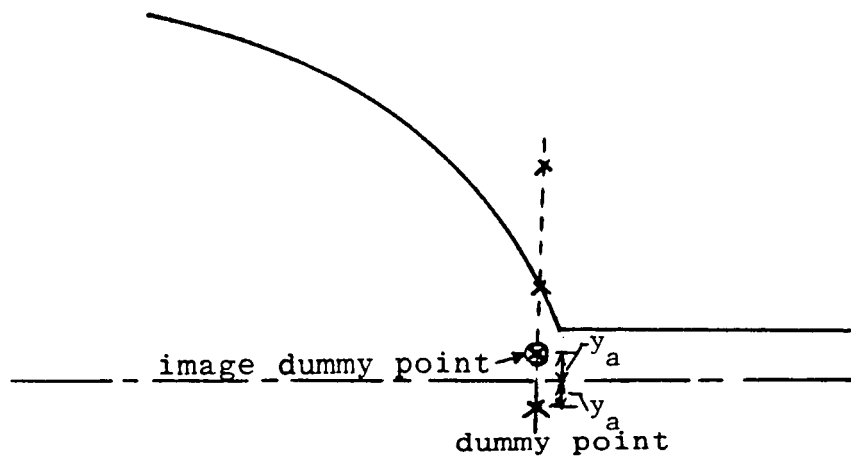
dummy point y_a

Figure 2b. Image Dummy Point inside the Body

image dummy point
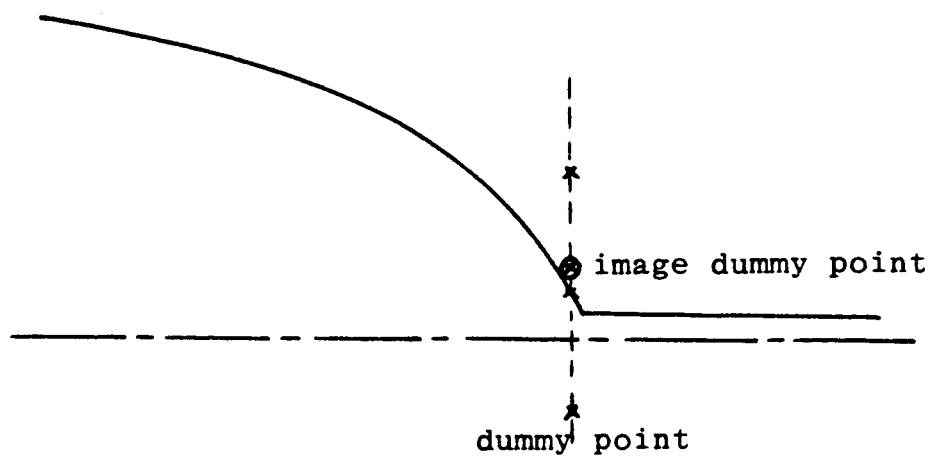
dummy point

Figure 2c. Image Dummy Point outside the Body
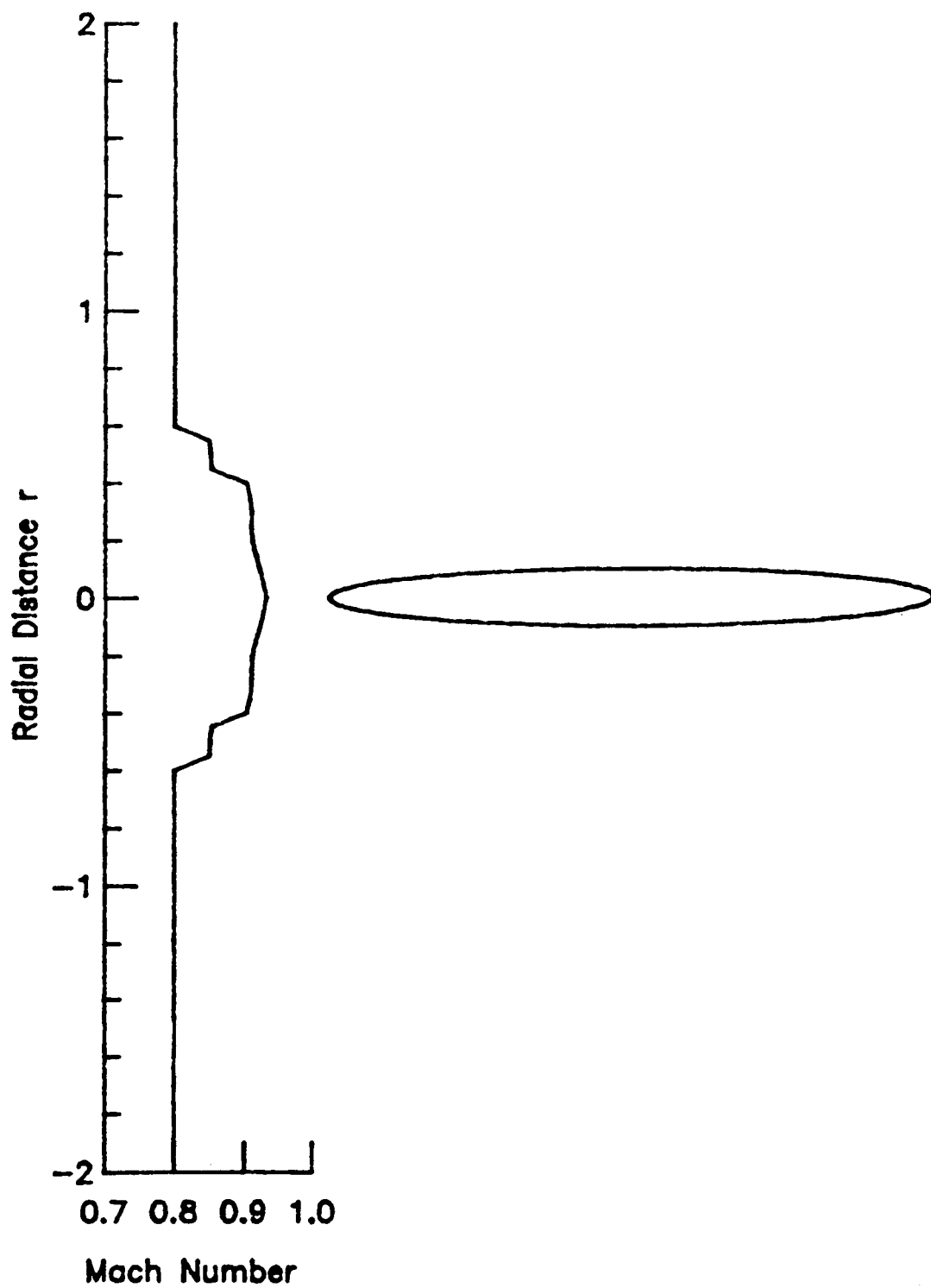
Figure 3.   Propfan Mach Number Profile and the
             the Relative Location of an Ellipsoid

Figure 4.   Propfan Slipstream Effect on
                Pressure Distribution of an Ellipsoid
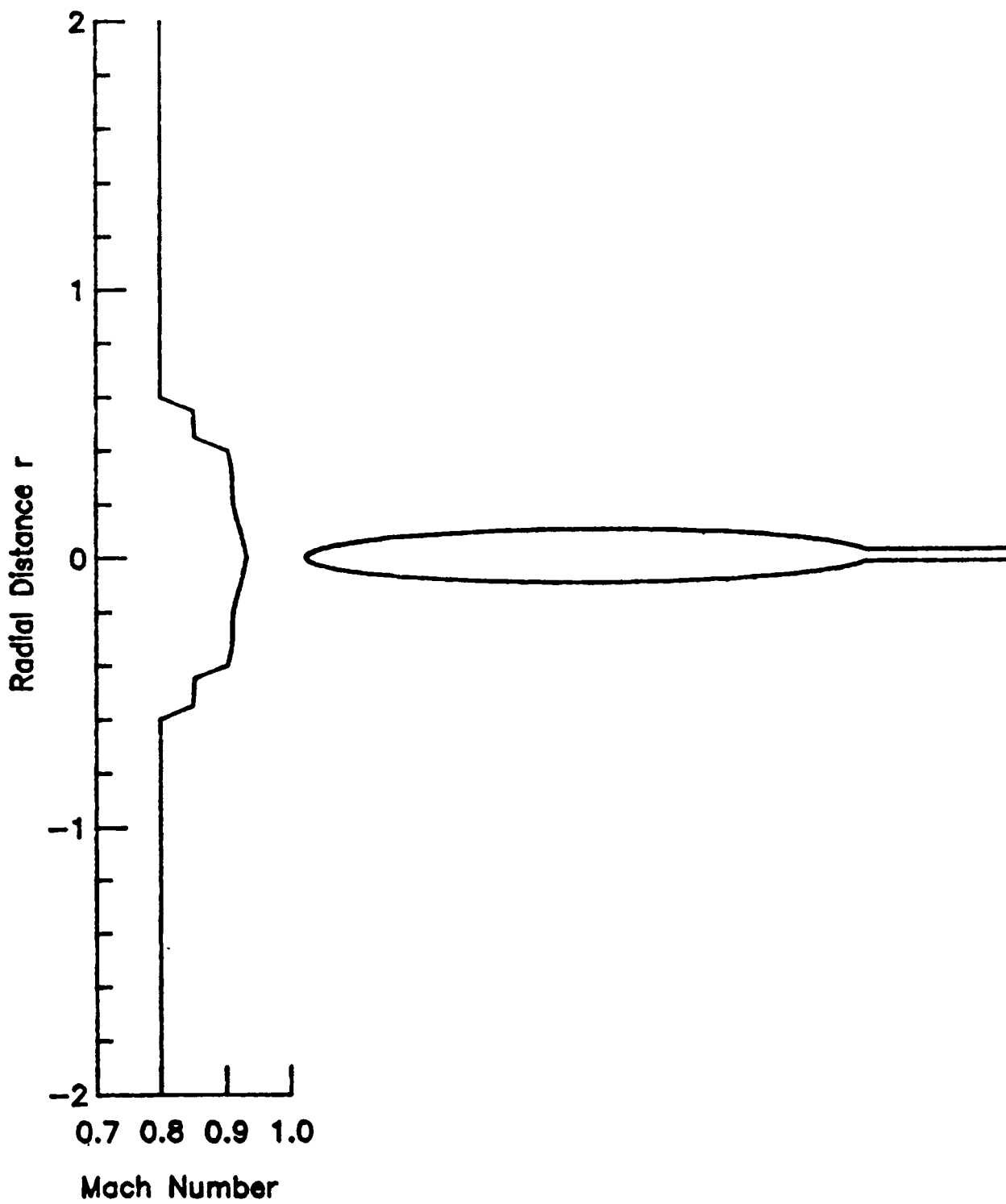
Figure 5. Propfan Mach Number Profile and the
Relative Location of an Ellipsoid/Sting
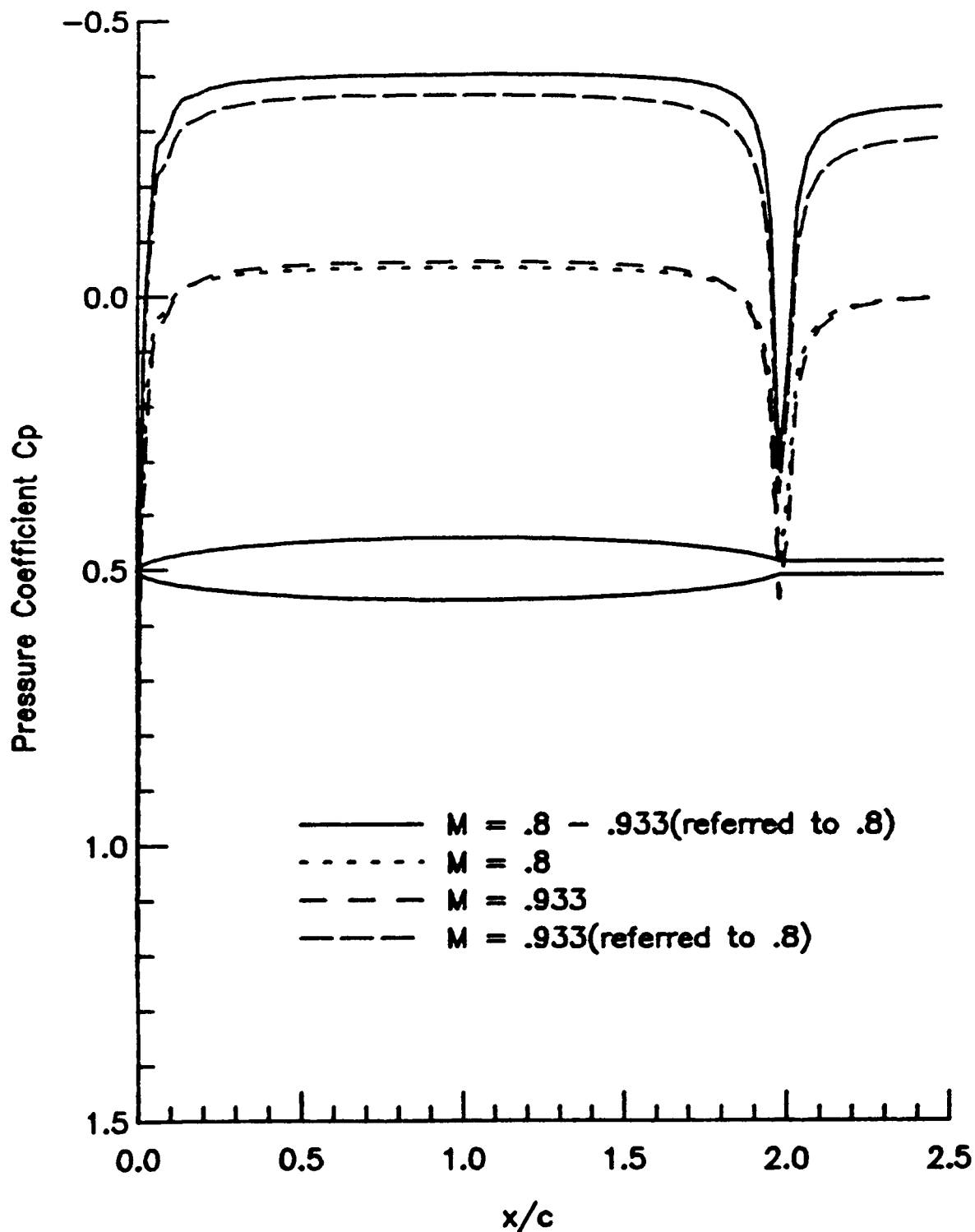
Figure 6. Propfan Slipstream Effect on Pressure
Distribution of an Ellipsoid/Sting
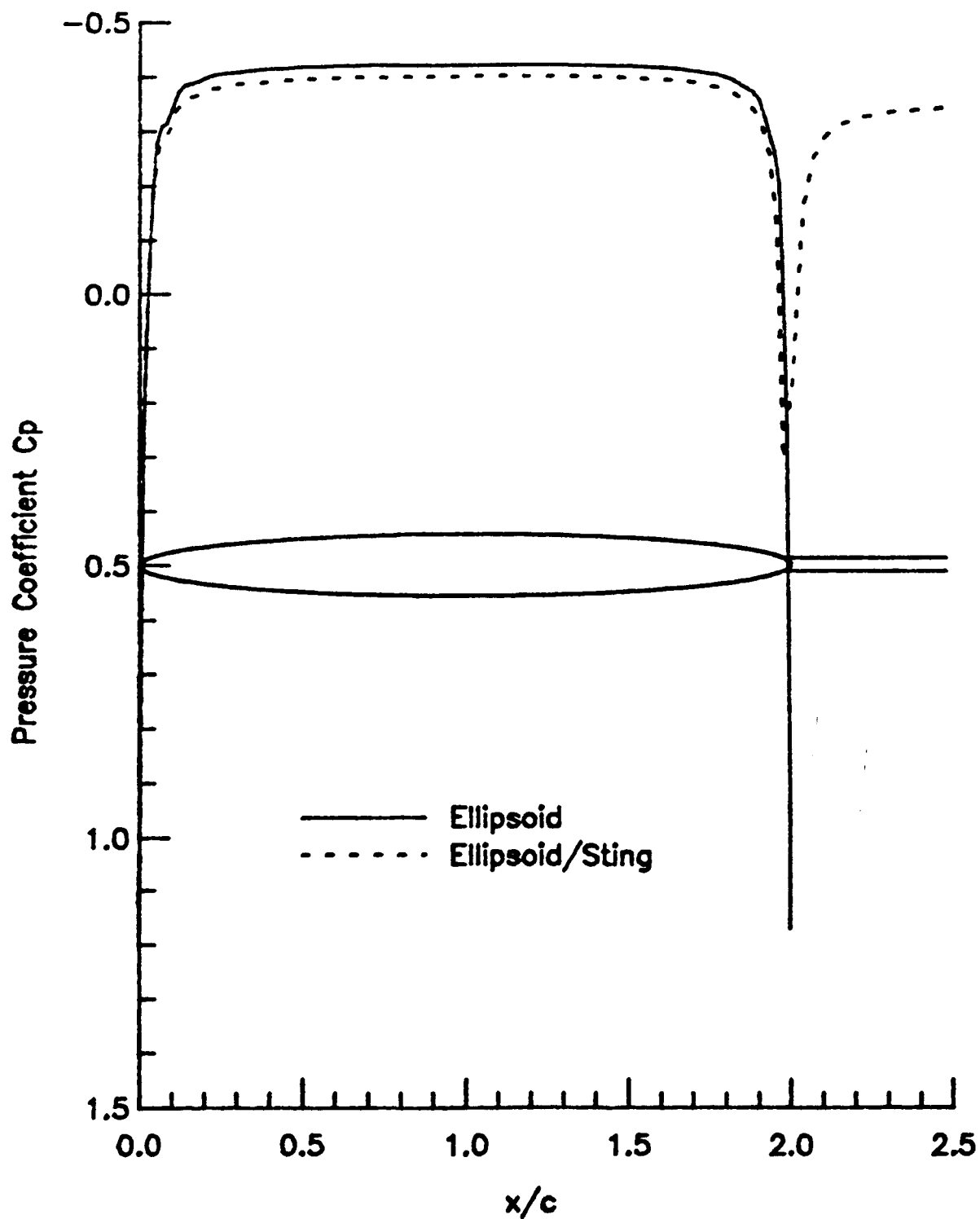
Figure 7. Comparison of Pressure Distributions
between Ellipsoids with and without Sting
in a Propfan Stream Given in Figure 5
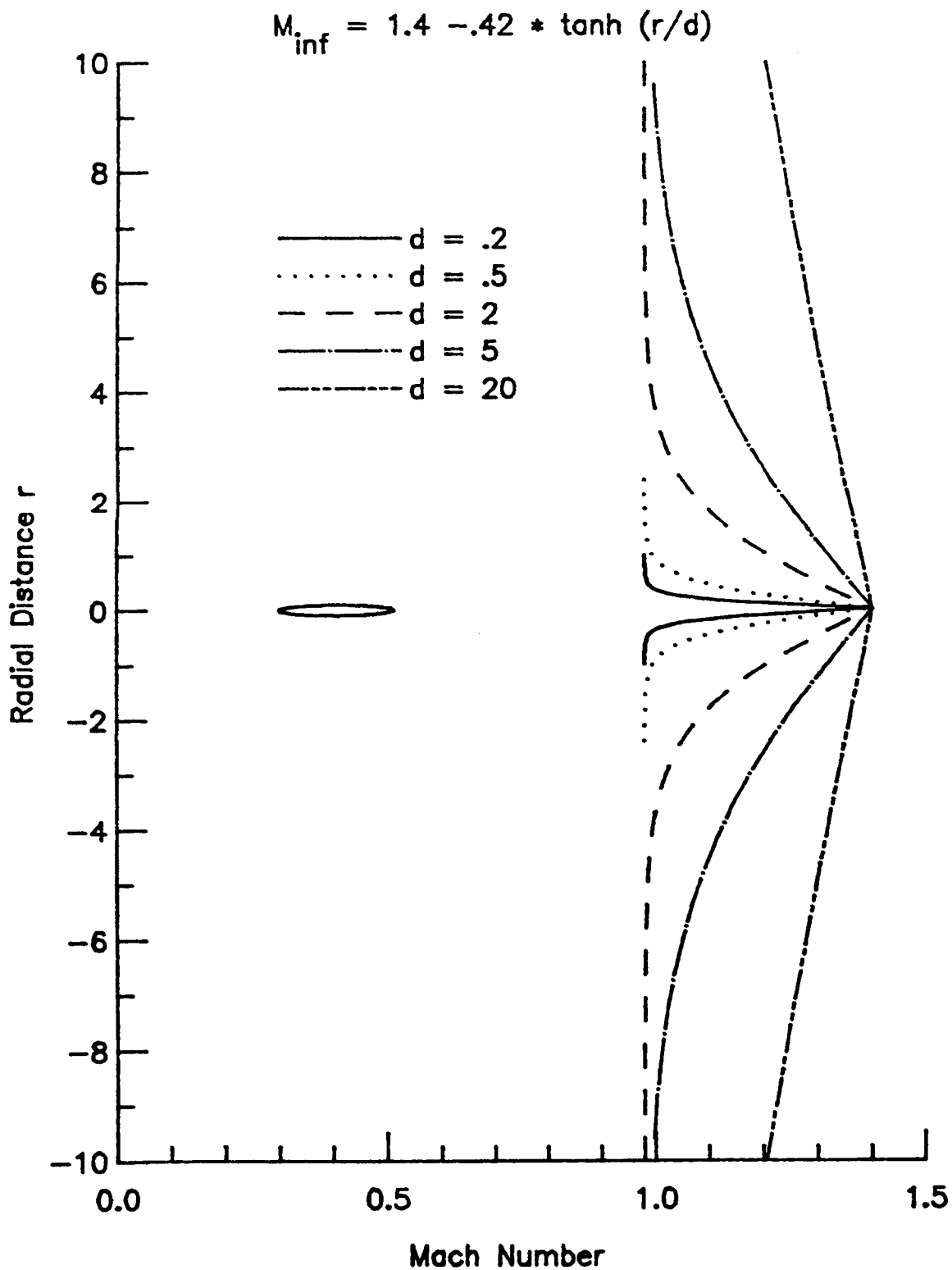
Figure 8a. Mach Number Profiles for Different Spread Parameters
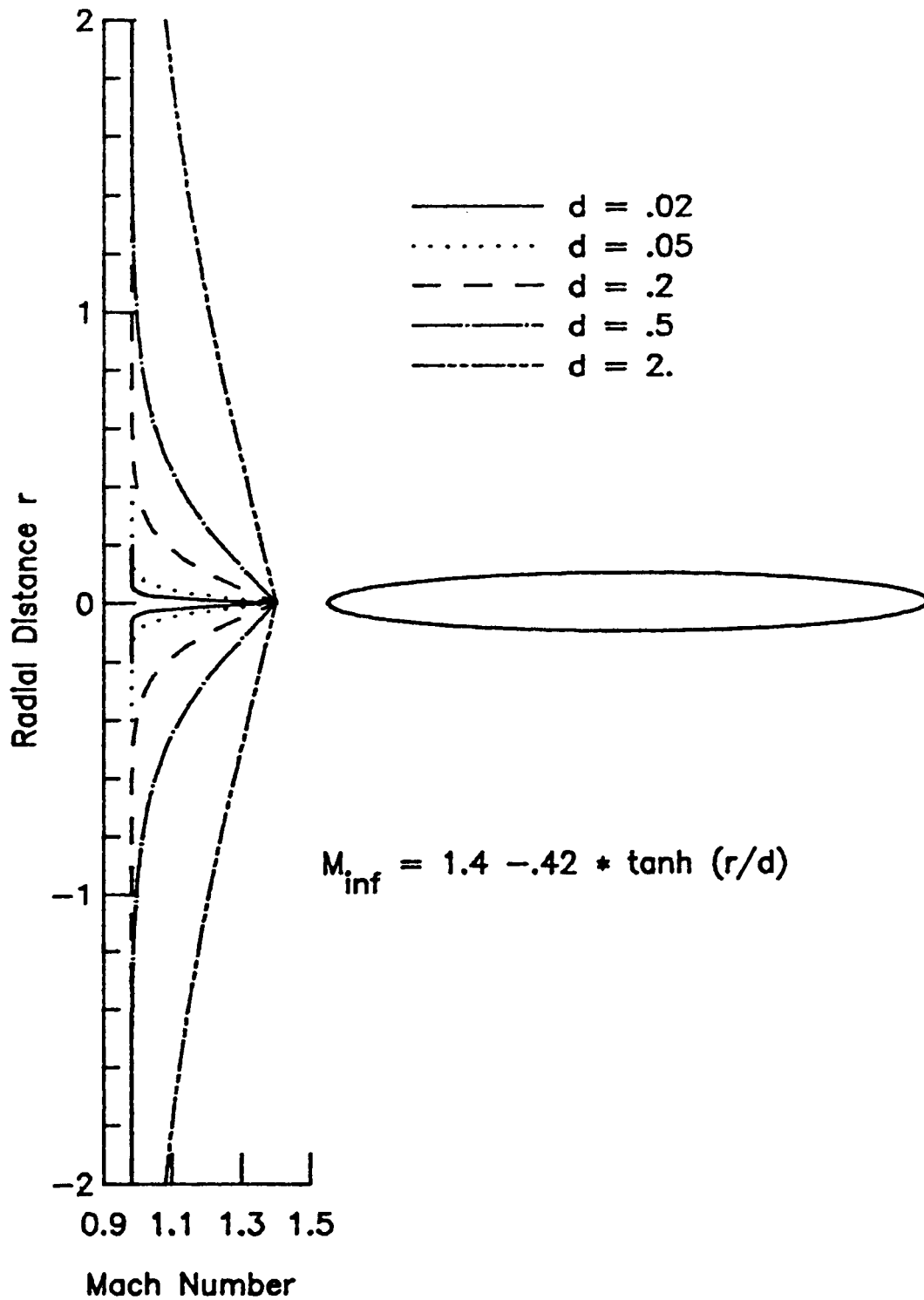
Figure 8b.   Mach Number Profiles for Different Spread Parameters

$$M_{inf} = 1.4 - .42 * \tanh (r/d)$$

d = .02
d = .05
d = .2
d = .5
d = 2.
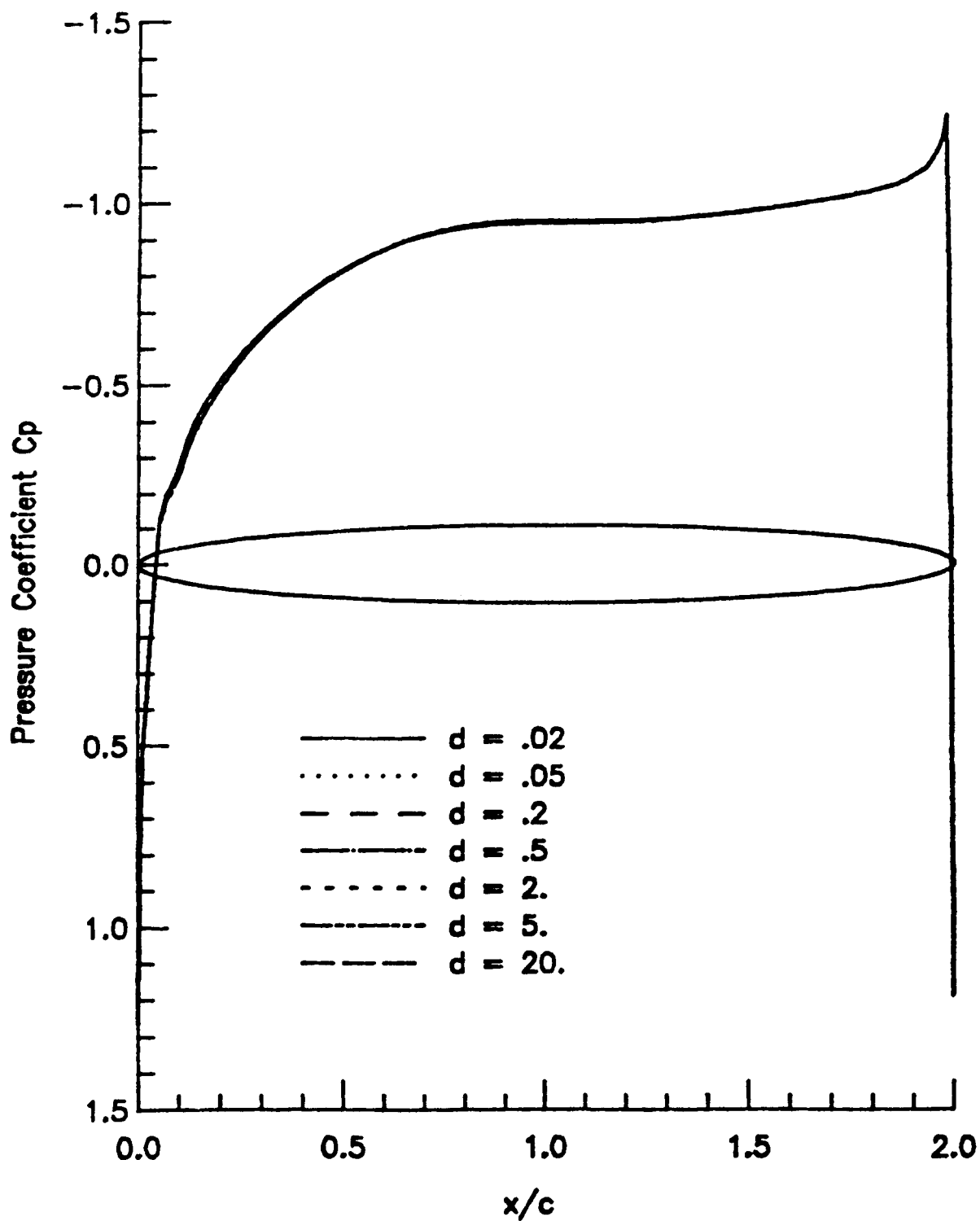
Figure 9. Spread Effect of Transonic Nonuniform Freestreams
on Pressure Distributions of an Ellipsoid
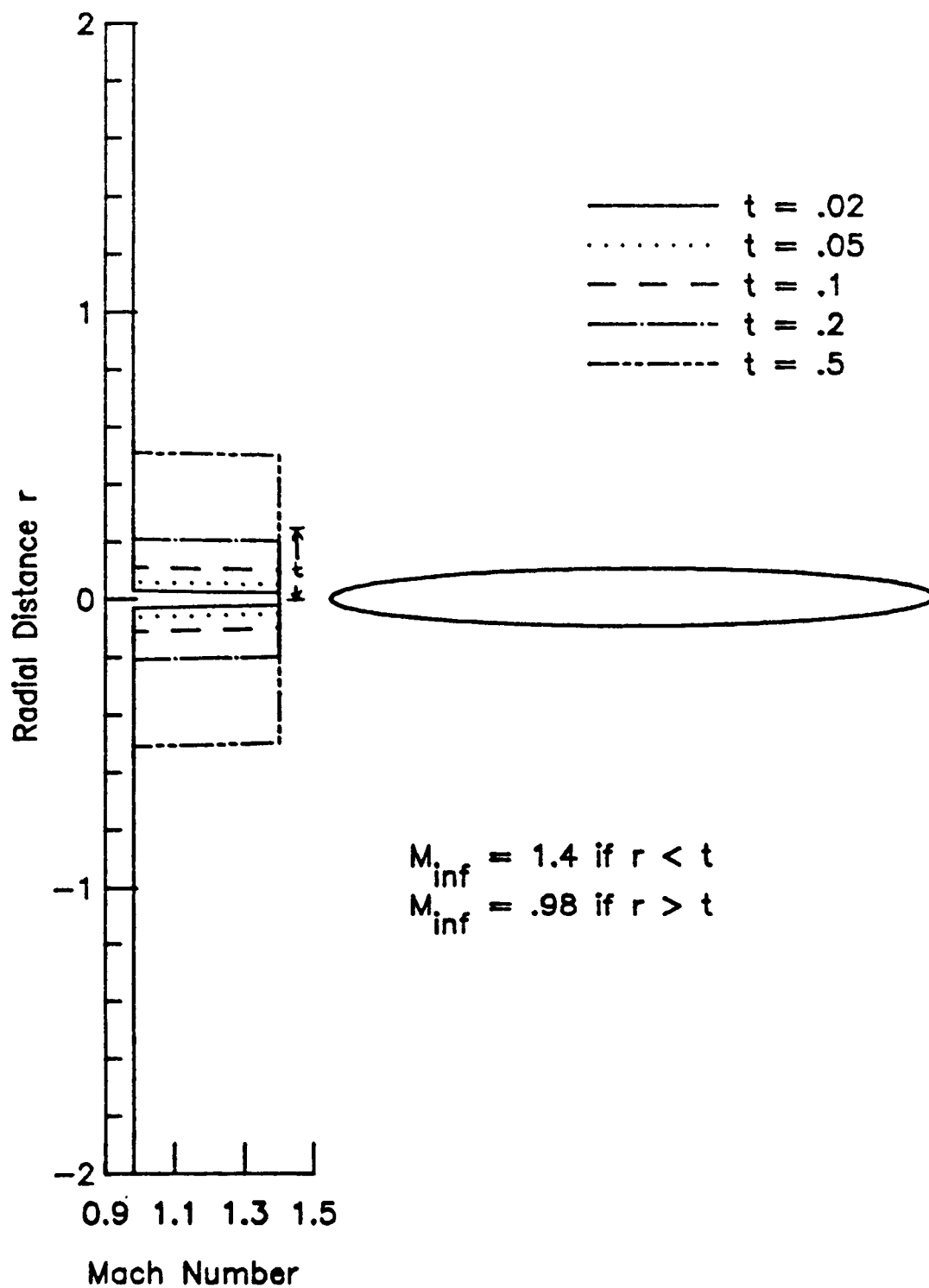
Figure 10. Mach Number Profiles for Different Nonuniformity Thickness
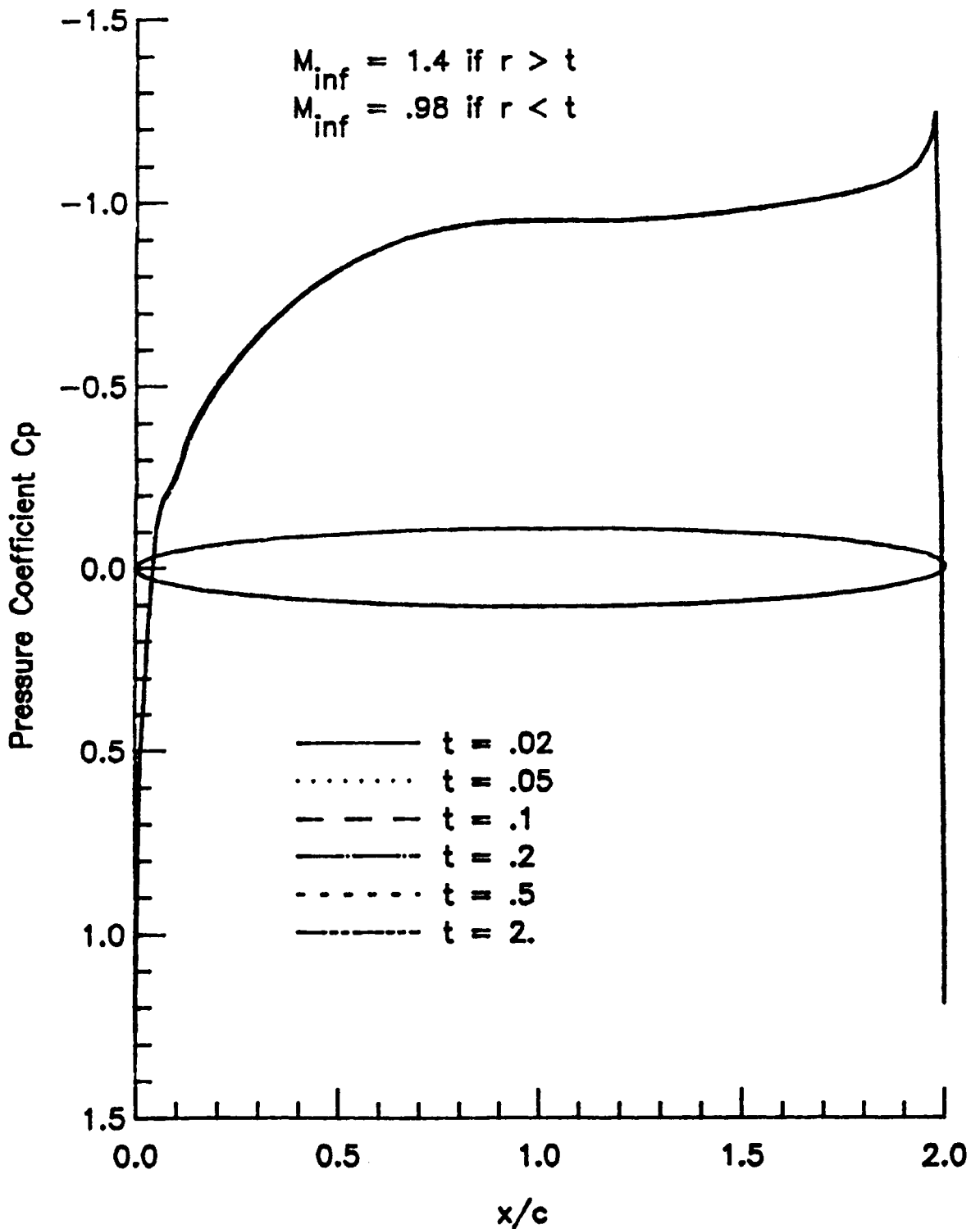
Figure 11. Depth Effect of Transonic Nonuniform Freestreams
on Pressure Distributions of an Ellipsoid

48
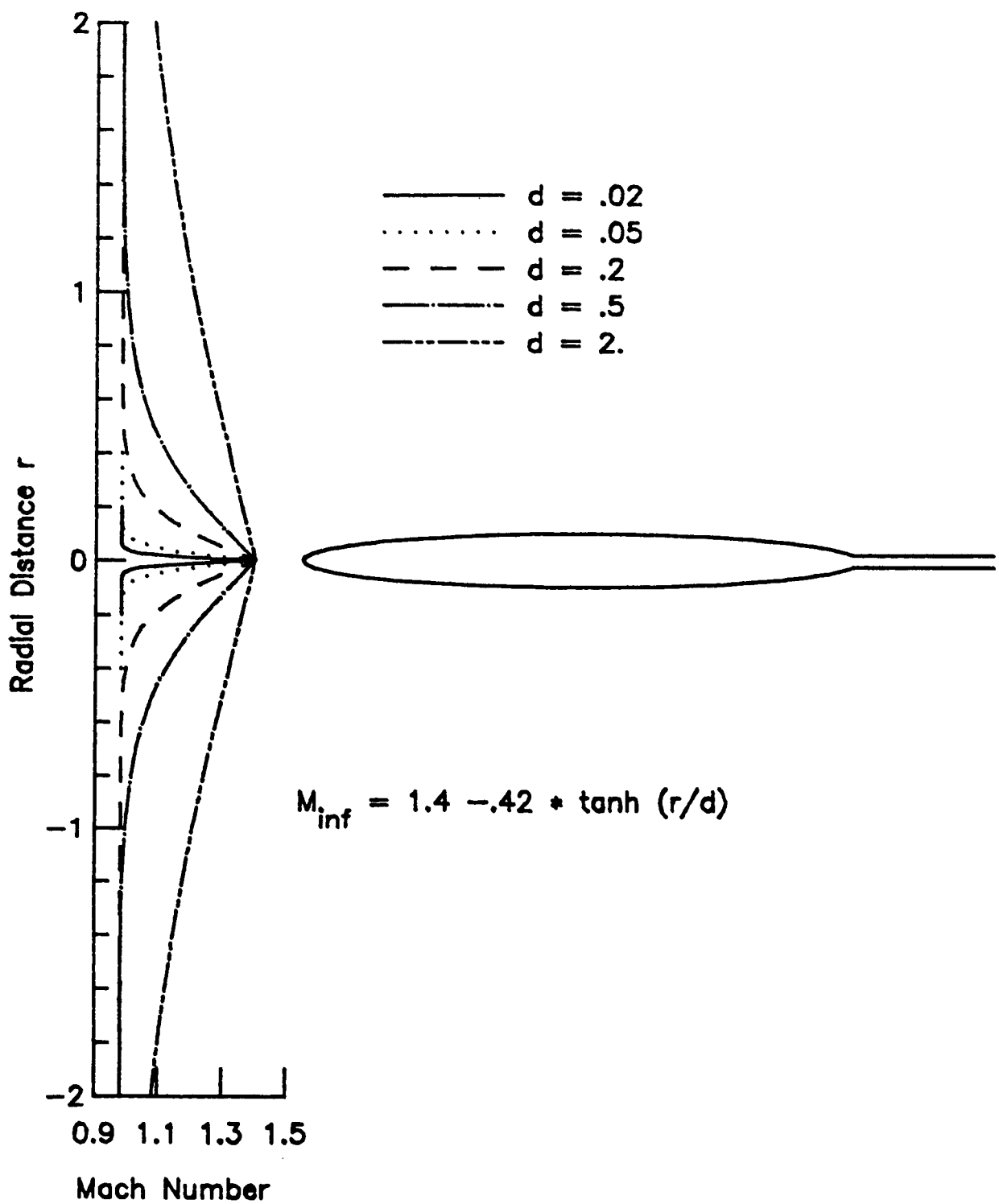
Figure 12. Mach Number Profiles for Different Spread Parameters

49
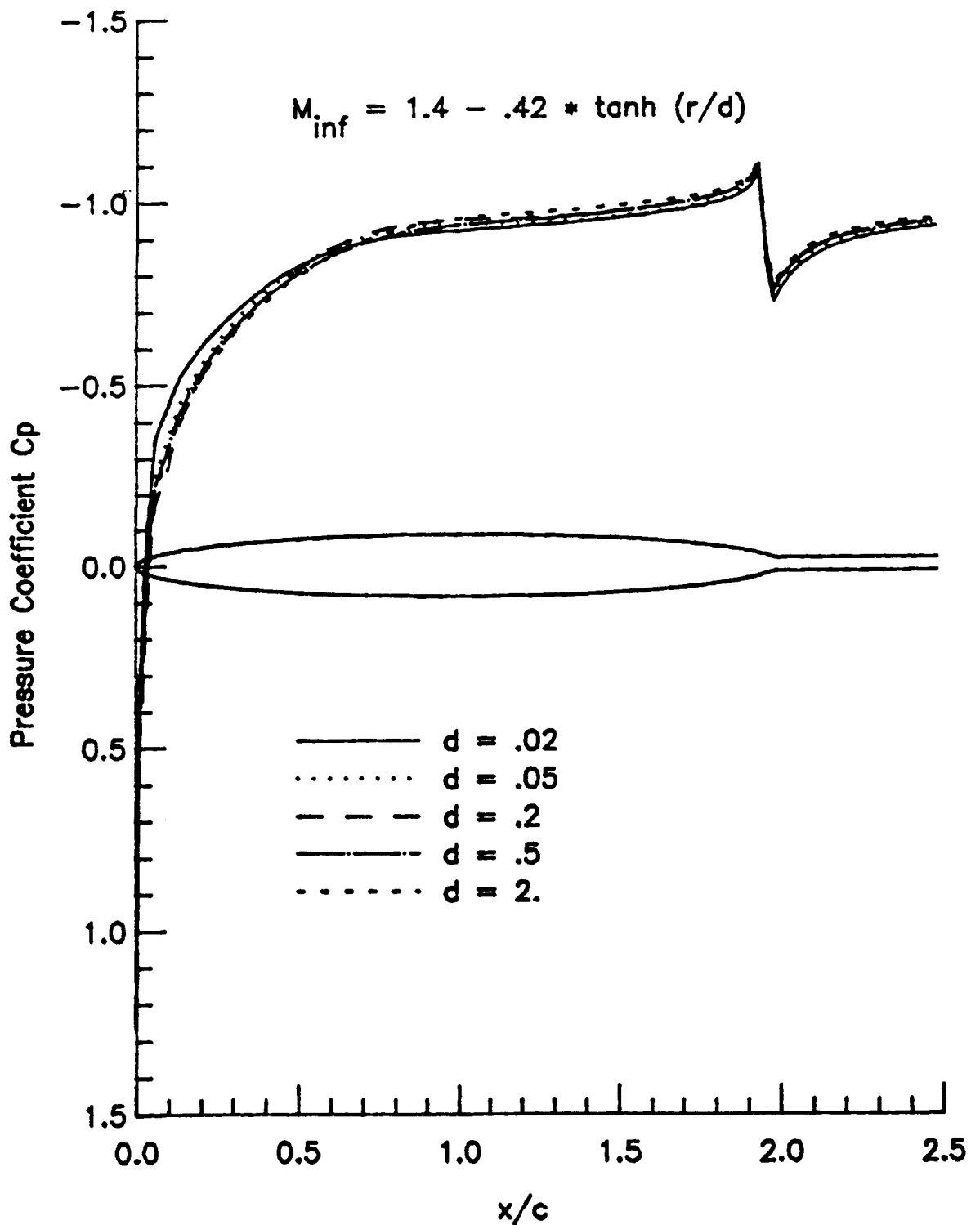
Figure 13. Spread Effect of Transonic Nonuniform Freestreams
on Pressure Distribution of an Ellipsoid/Sting
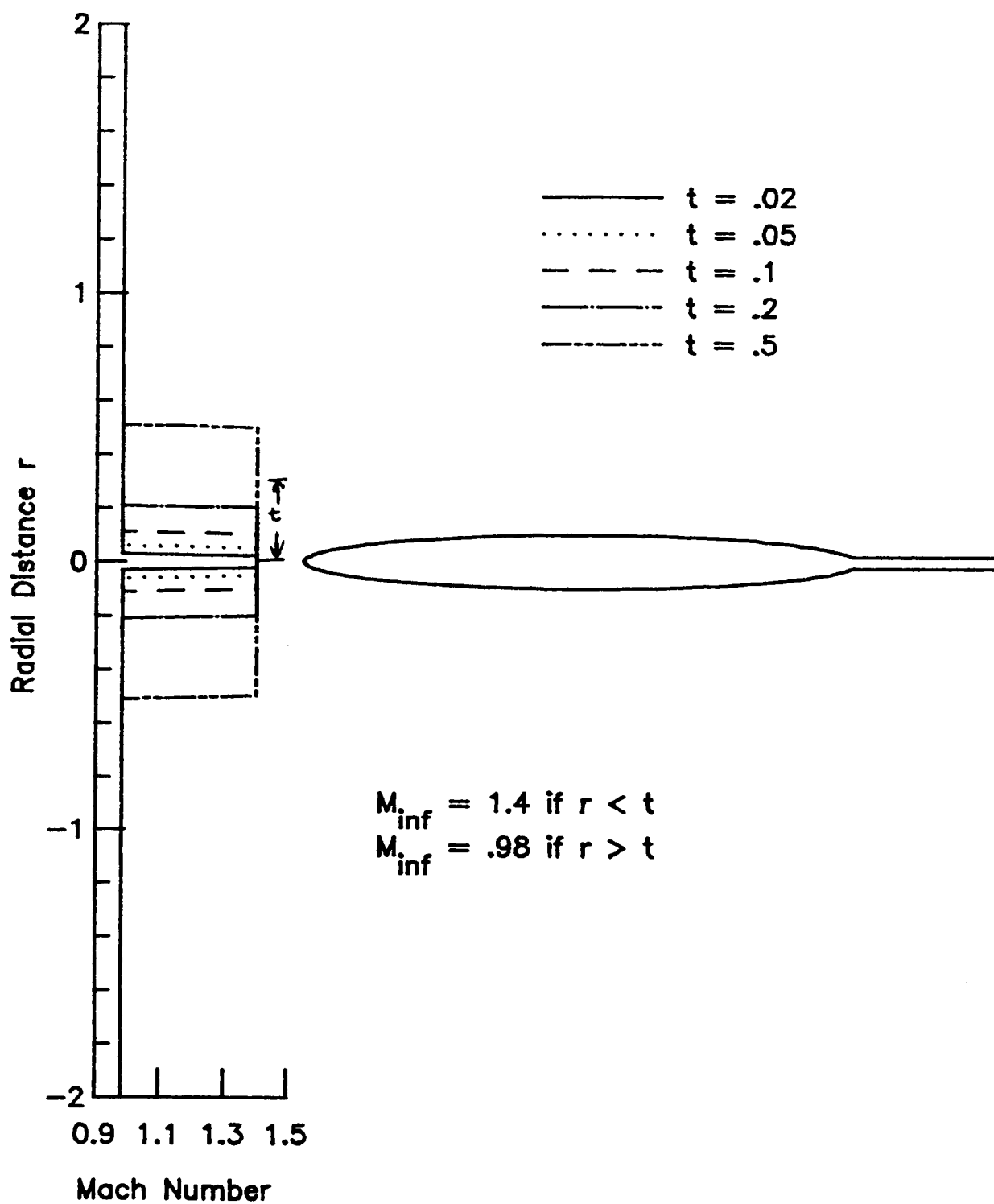
Figure 14. Mach Number Profiles for Different Nonuniformity Thickness
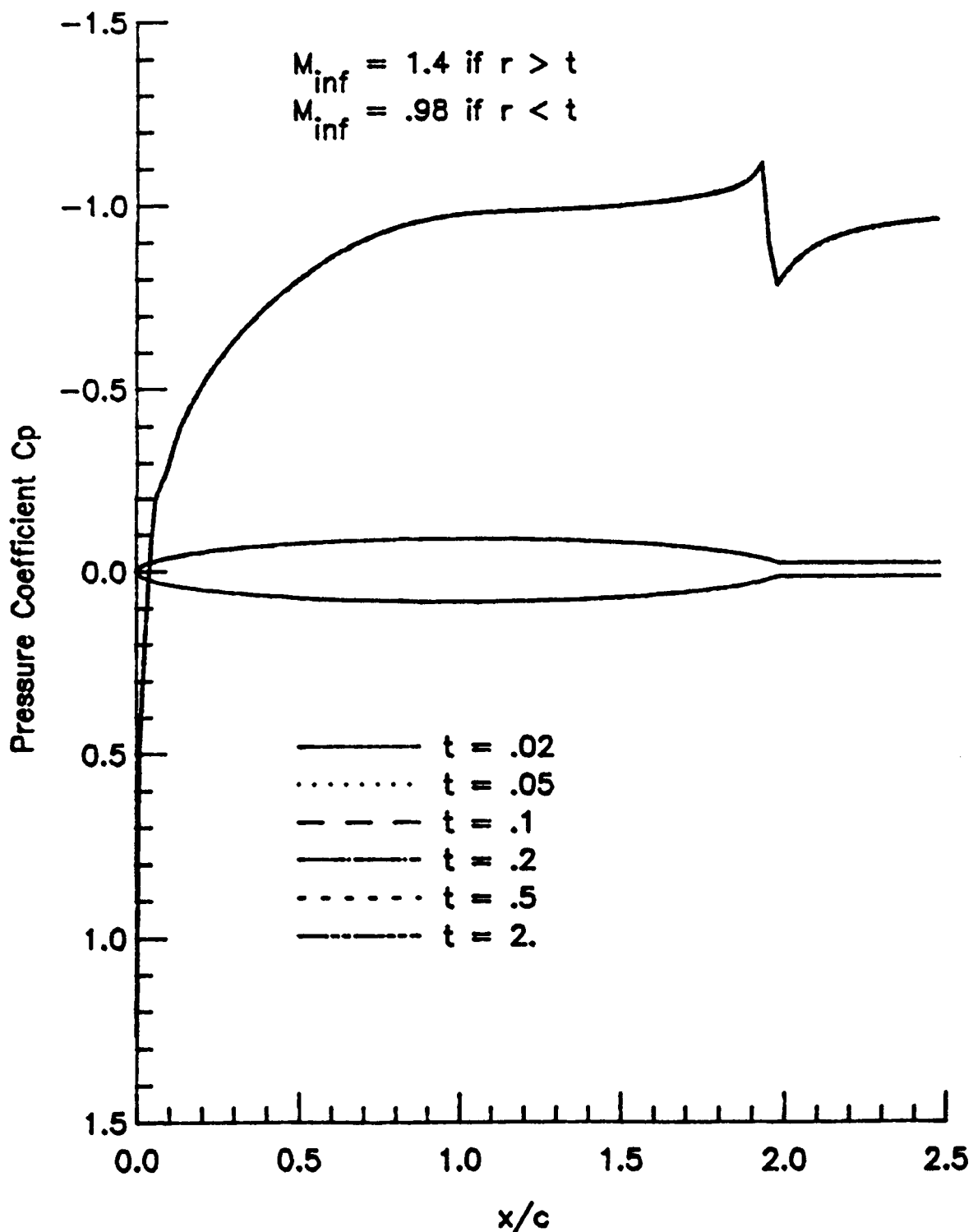
Figure 15. Depth Effect of Transonic Nonuniform Freestreams on Pressure Distribution of an Ellipsoid/Sting

$$M_{inf} = 1.4 - .42 * \tanh(r/d)$$
$$M_{inf} = 1.4 \text{ if } r > t$$
$$M_{inf} = .98 \text{ if } r < t$$

Ellipsoid (d = .2)
Ellipsoid (t = .2)
Ellipsoid/Sting (d = .2)
Ellipsoid/Sting (t = .2)
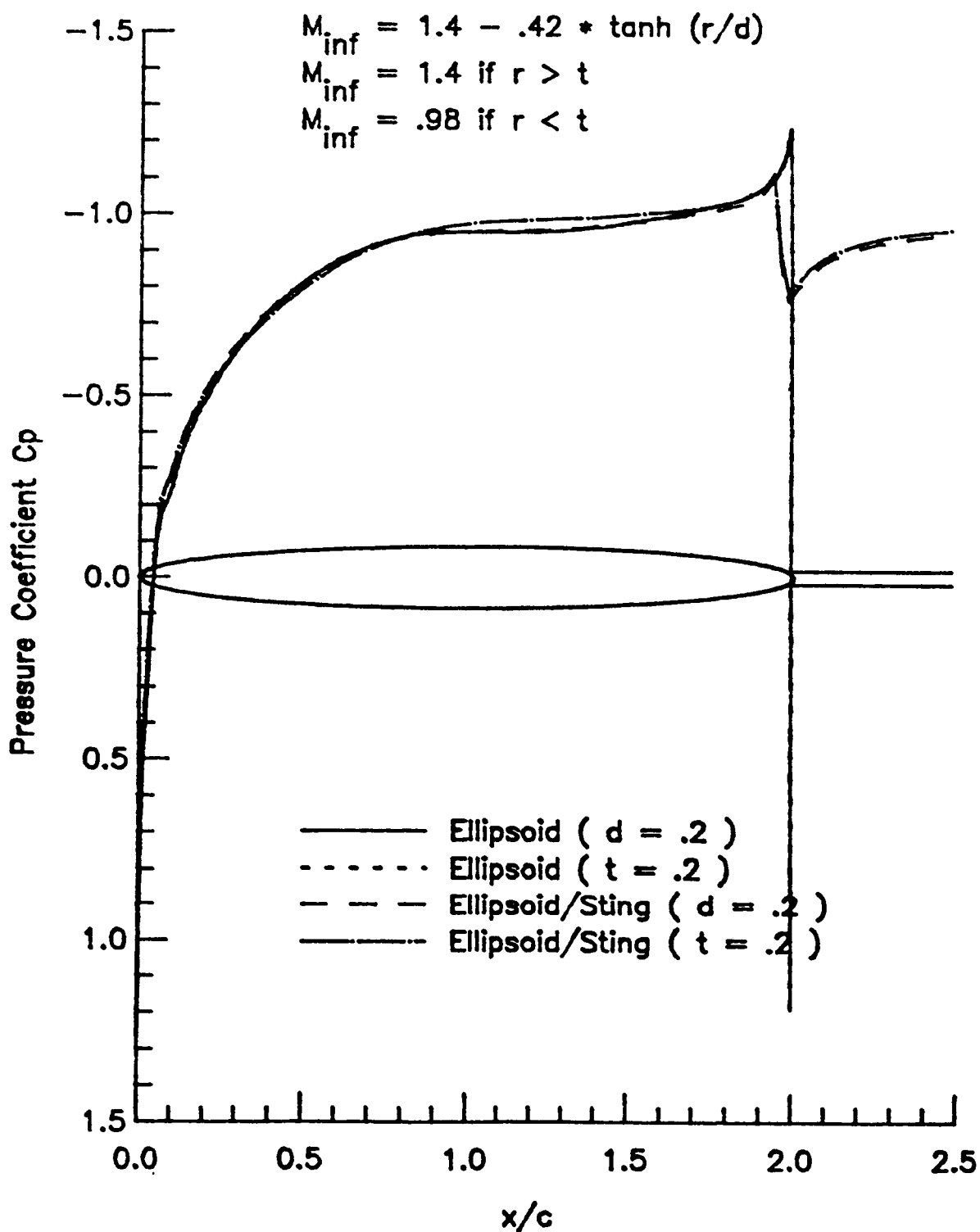
Figure 16. Comparison of Pressure Distributions
between Ellipsoids with/without a Sting
and Different Types of Nonuniformities

$$M_{inf} = M_{high} - M_{diff} * tanh\ (r/.2)$$

Legend:
- — · — Mach 1.1
- ——— Mach 1.1 — 1.2
- ·········· Mach 1.1 — 1.3
- — — — Mach 1.1 — 1.4

Y-axis: Pressure Coefficient Cp

X-axis: x/c
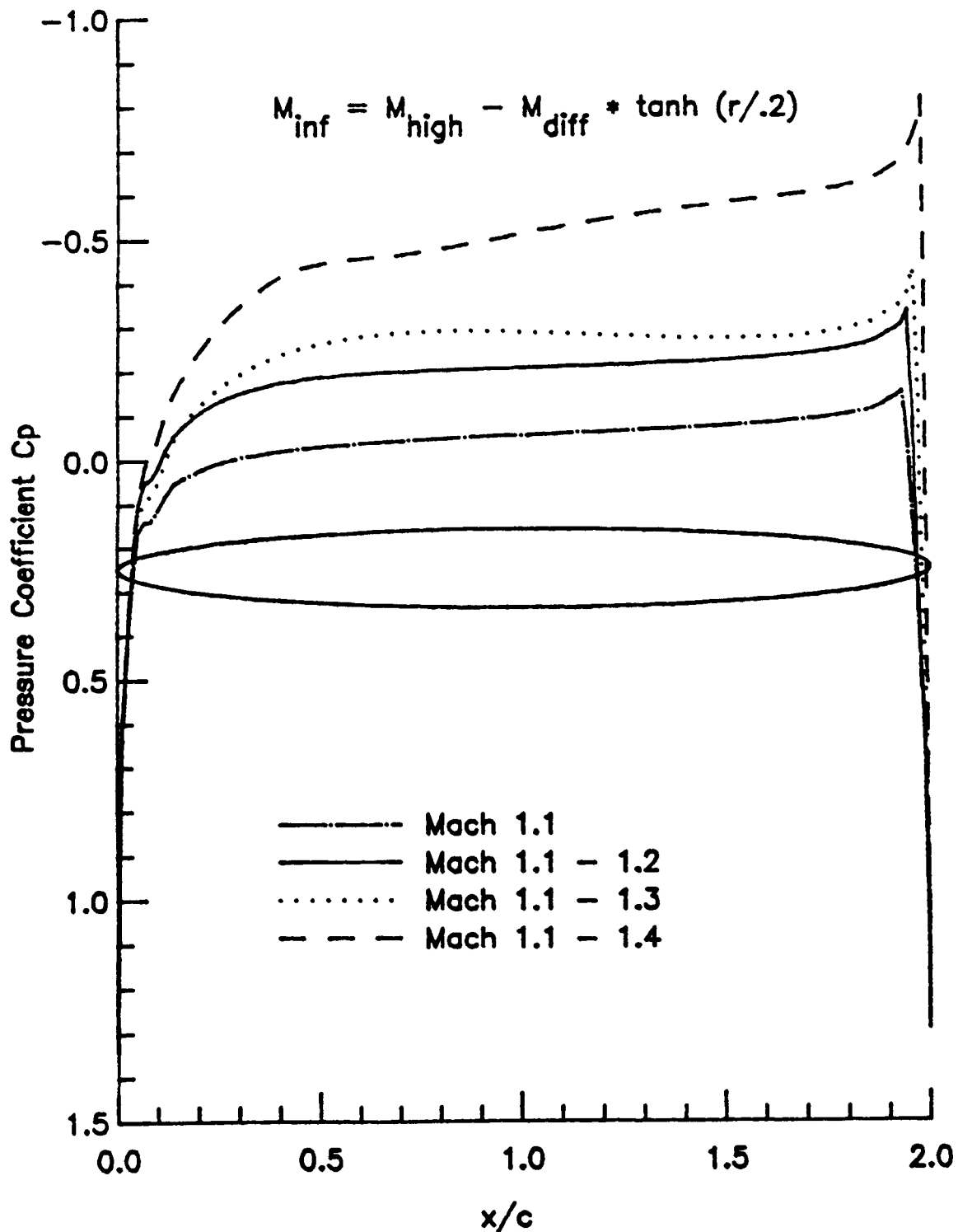
Figure 17. Effect of Supersonic Nonuniform Freestreams
on Pressure Distribution of an Ellipsoid

$$M_{inf} = M_{high} - M_{diff} * \tanh (r/.2)$$

Legend:
- Mach 1.1
- Mach 1.1 − 1.2
- Mach 1.1 − 1.3
- Mach 1.1 − 1.4

x/c
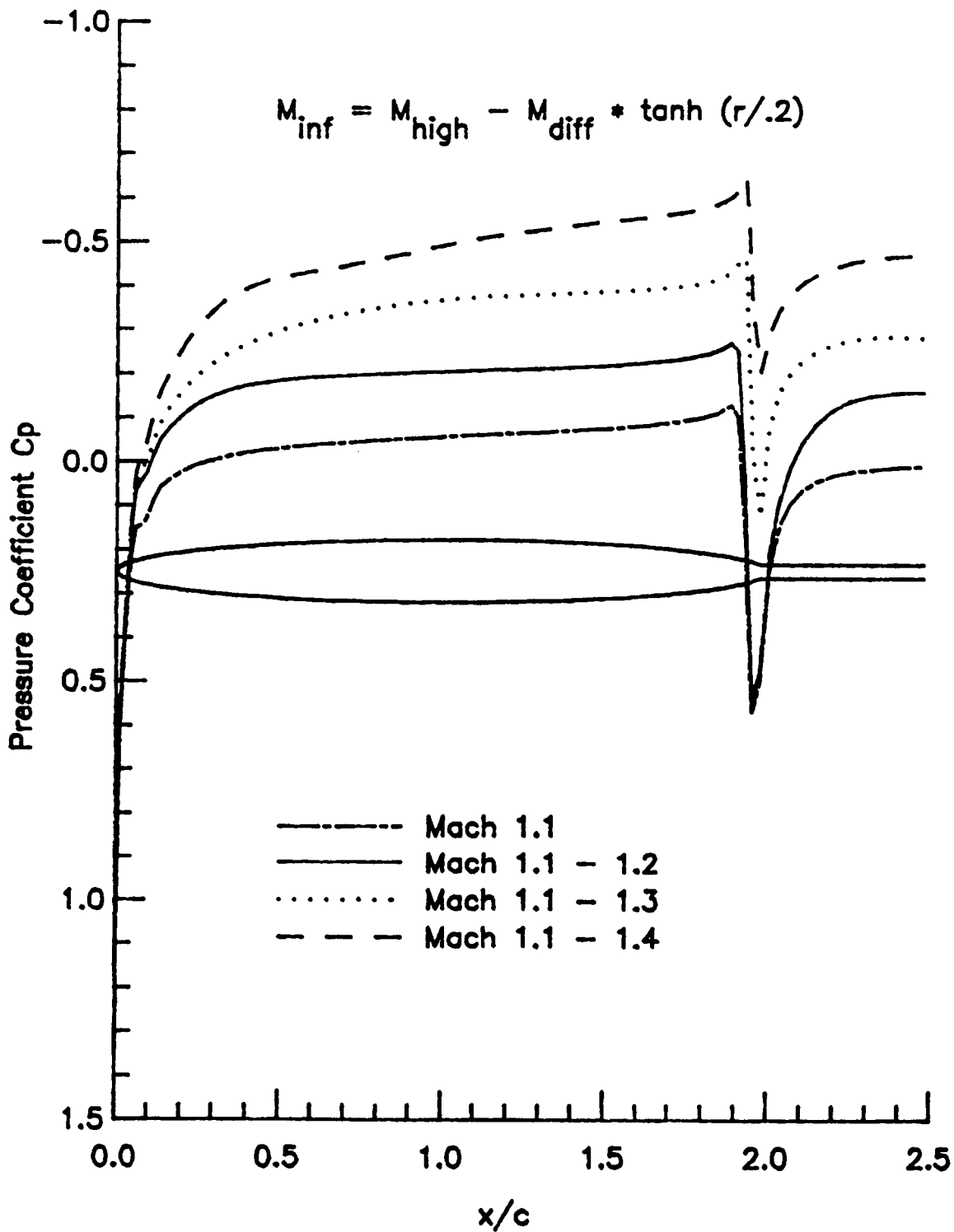
Figure 18. Effect of Supersonic Nonuniform Freestreams
on Pressure Distribution of an Ellipsoid/Sting

$$M_{inf} = M_{high} - M_{diff} * \tanh (r/.2)$$

Legend:
- · · · · · Mach .98
- —— Mach .98 − 1.1
- · · · · · Mach .98 − 1.2
- — — Mach .98 − 1.3
- —·—·— Mach .98 − 1.4
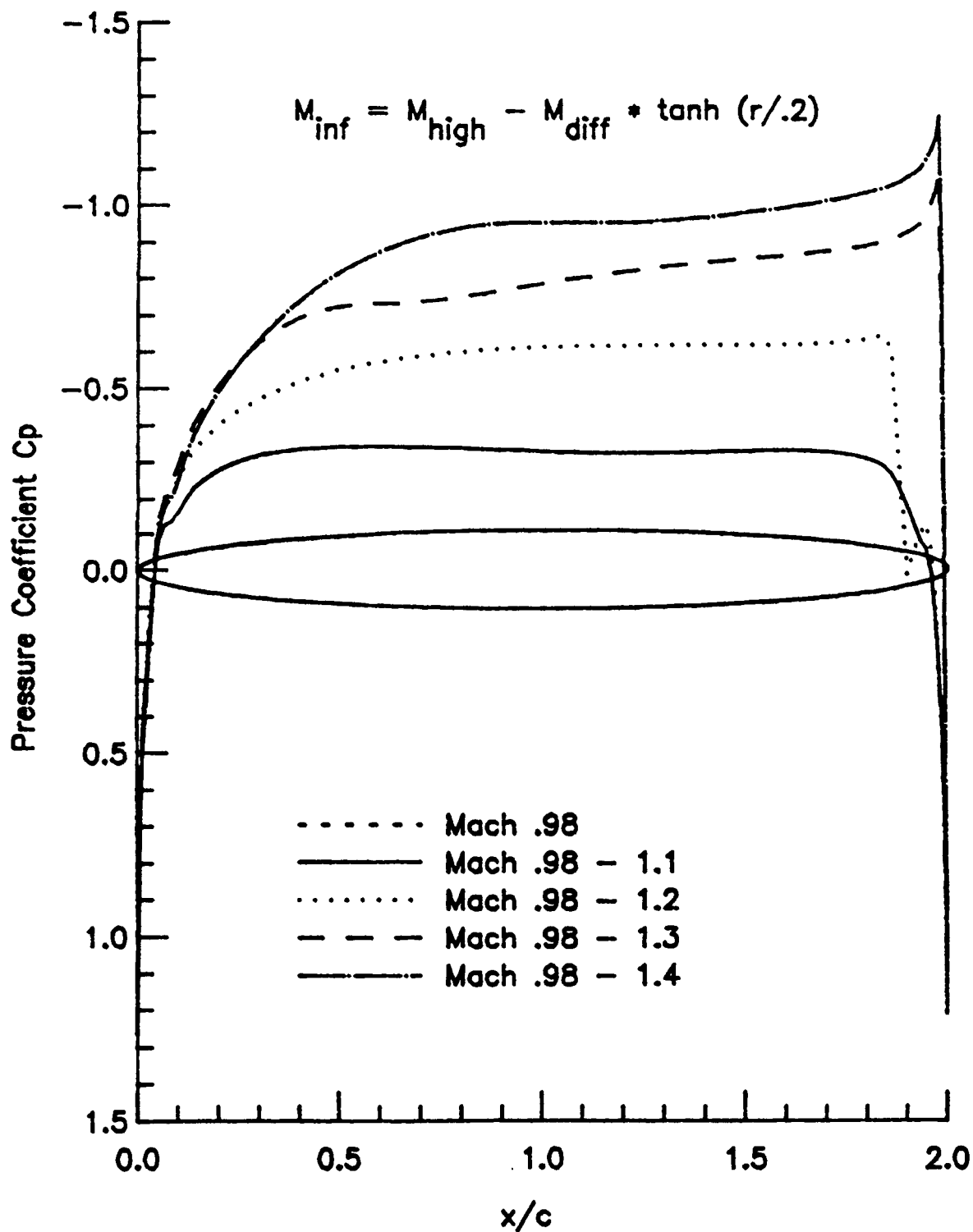
Figure 19. Effect of Transonic Nonuniform Freestreams on Pressure Distribution of an Ellipsoid

Figure 20. Effect of Transonic Nonuniform Freestream on Pressure Distribution of an Ellipsoid/Sting

$$M_{inf} = 1.4 - M_{diff} * \tanh(r/.2)$$
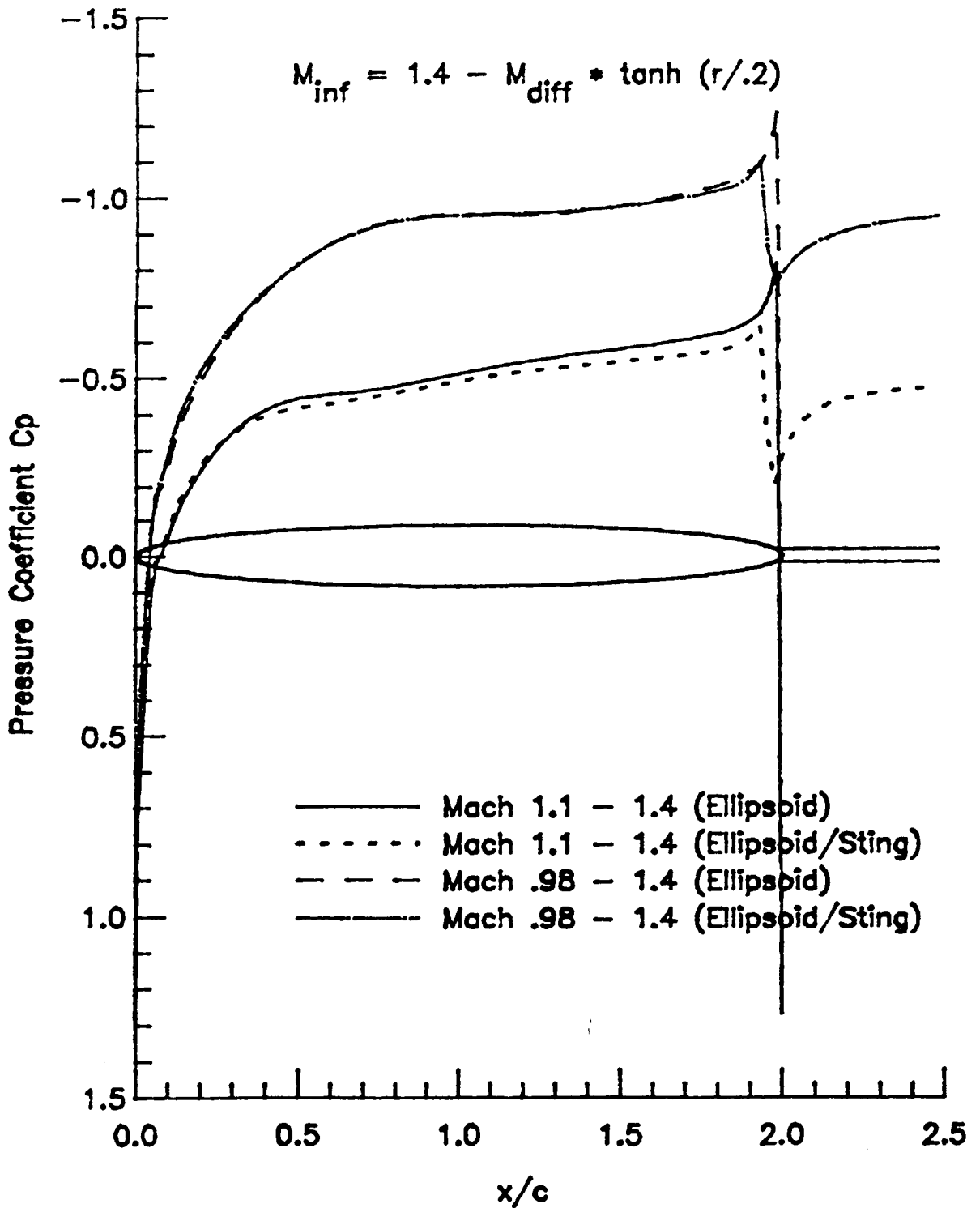
Figure 21. Comparison of Pressure Distributions of Ellipsoids with/without Sting in Supersonic and Transonic Free Stream
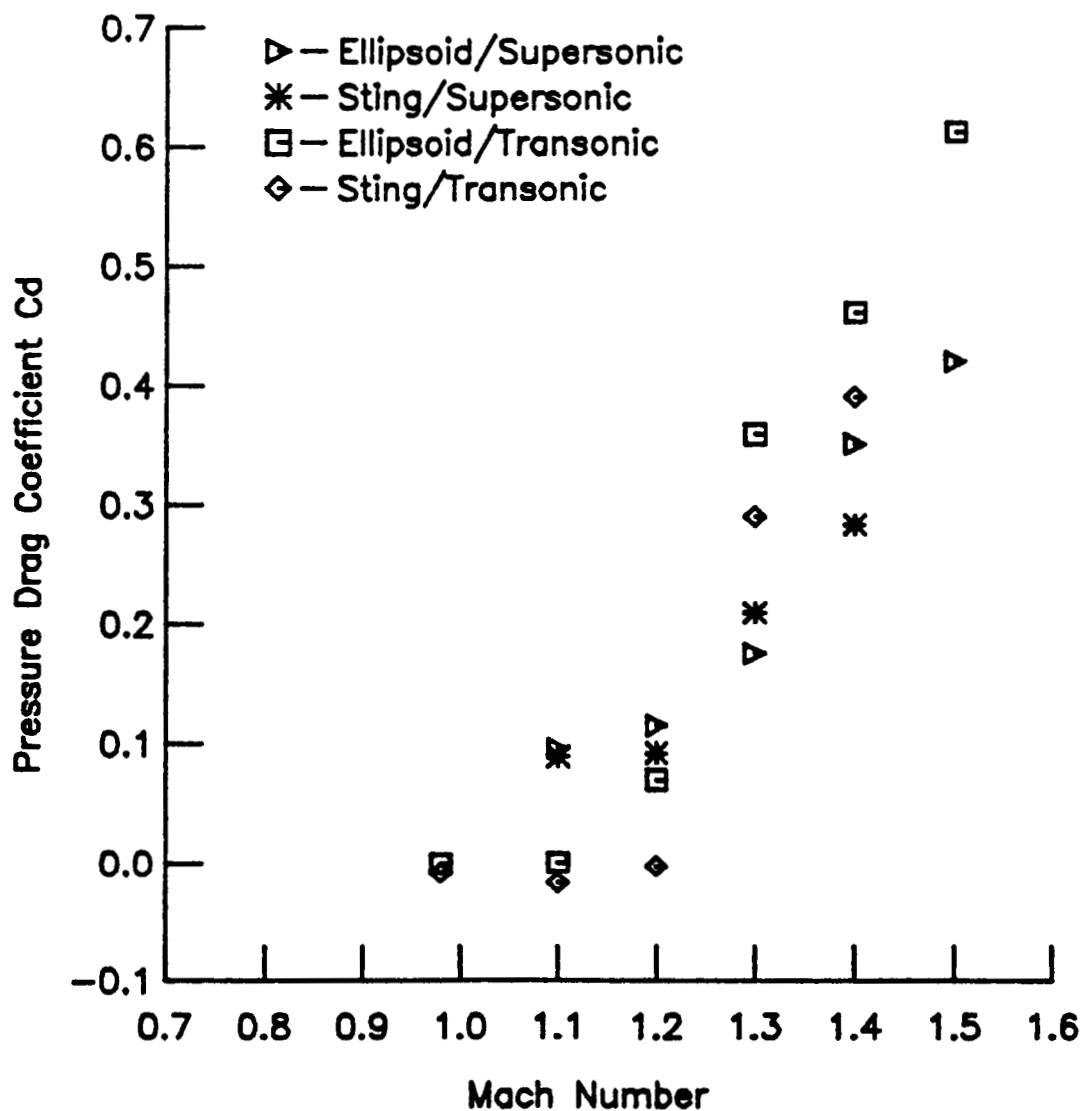
Figure 22. Effect of Nonuniformity Magnitude on Drag Coefficient. Symbols at Higher Mach Numbers Represent the Condition of Uniform Flow. Symbols at Higher Mach Numbers Represent Nonuniform Flow With Maximum Mach Numbers at the Indicated Values.
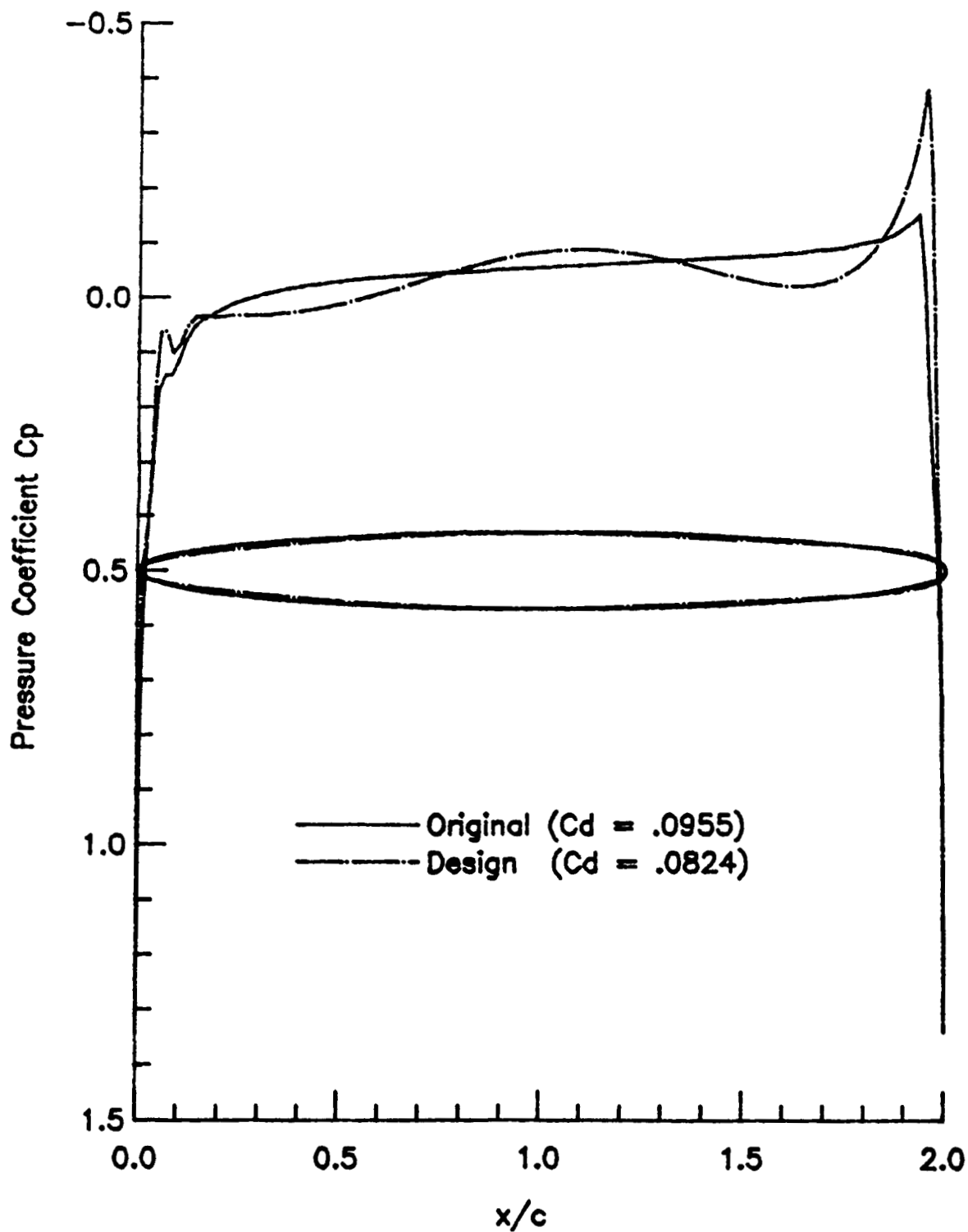
Figure 23. Comparison of Original and Design Shapes and Pressure Distributions in Uniform Flow of M=1.1
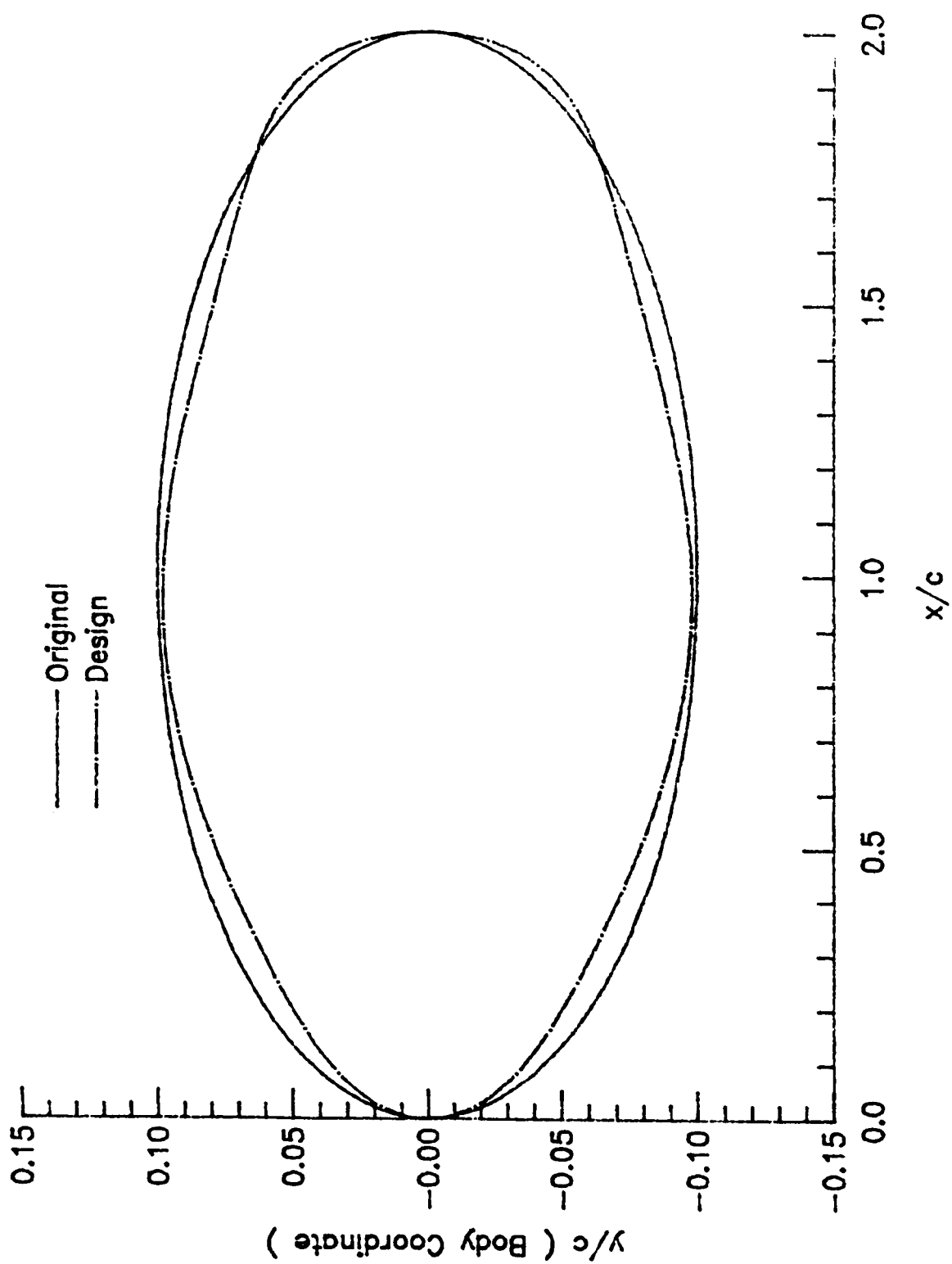
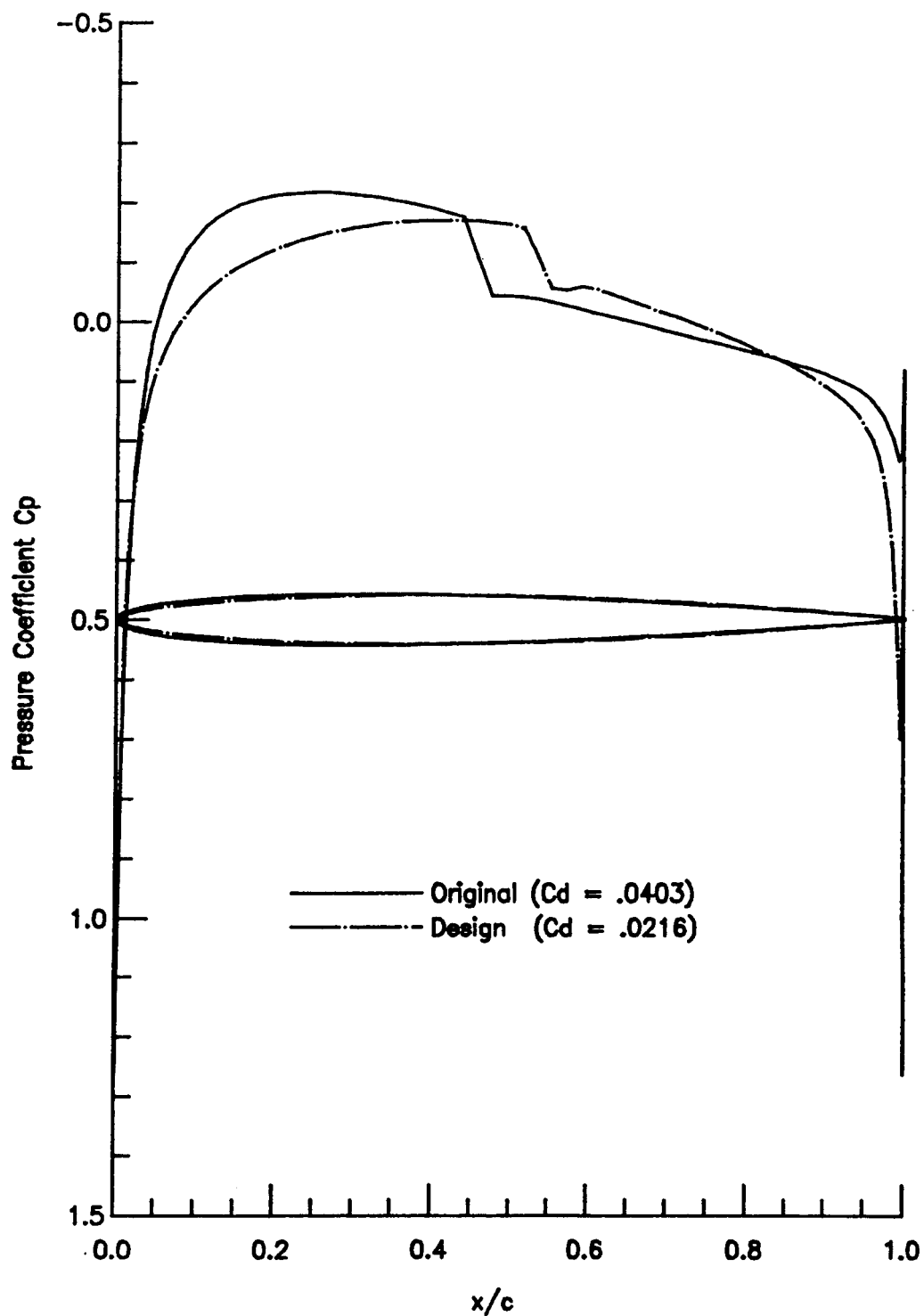Figure 24. Comparison of Original and Design Shapes in a Supersonic Uniform Flow (M = 1.1)

61
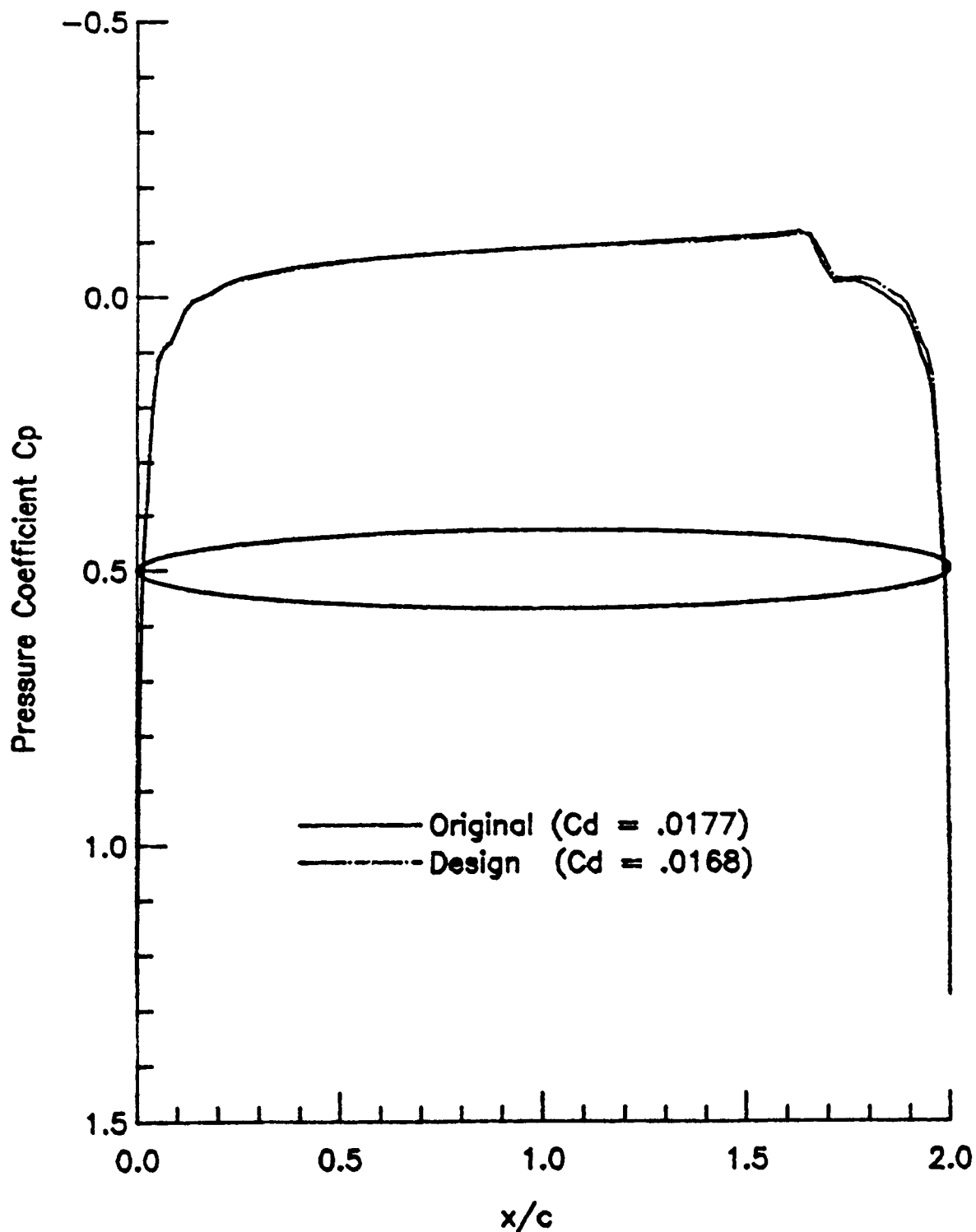
Figure 25.   Comparison of Original and Design Shapes and
Pressure Distributions in Uniform Flow of M=.995
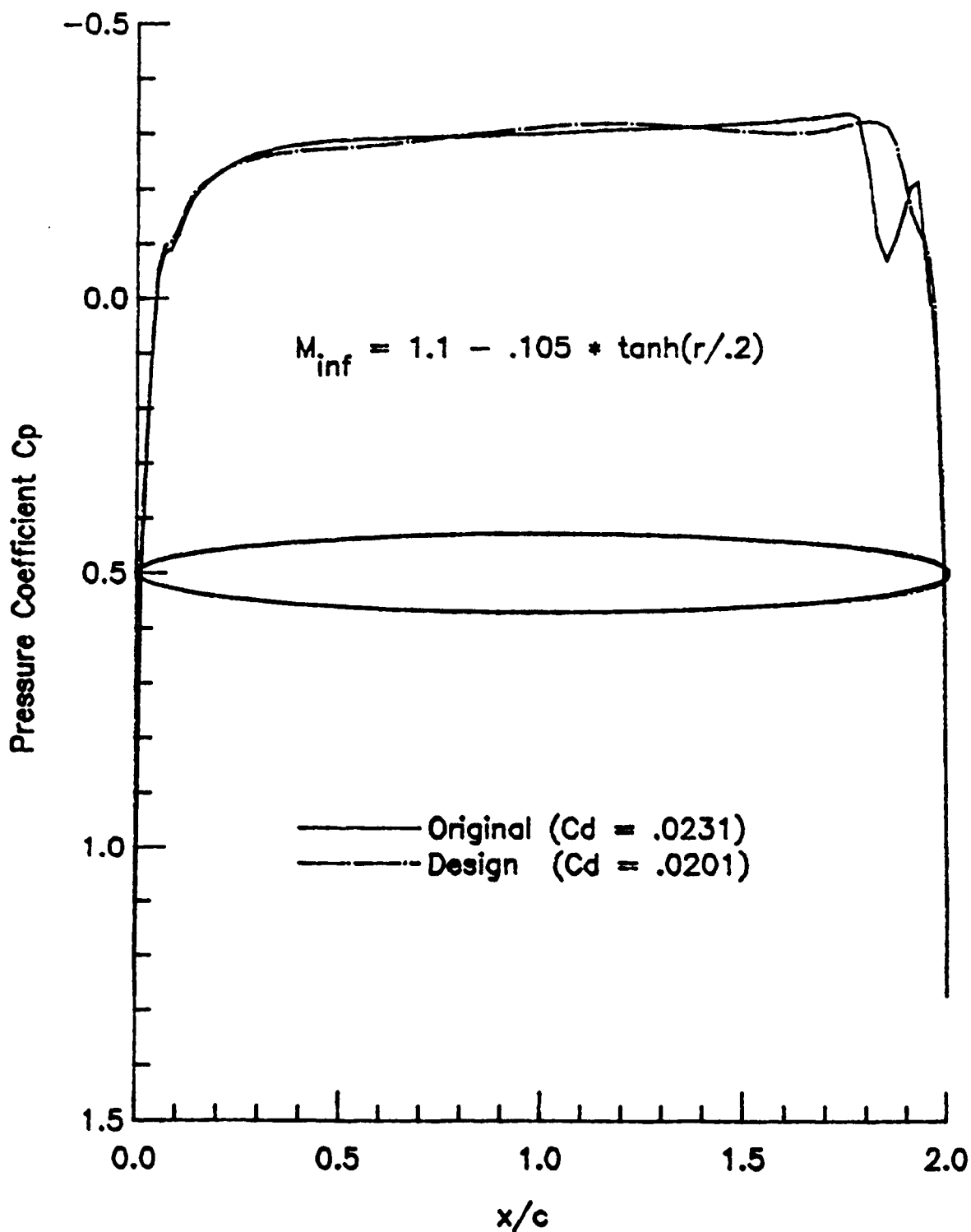
Figure 27. Comparison of Original and Design Shapes and Pressure Distributions in a Transonic Nonuniform Freestream
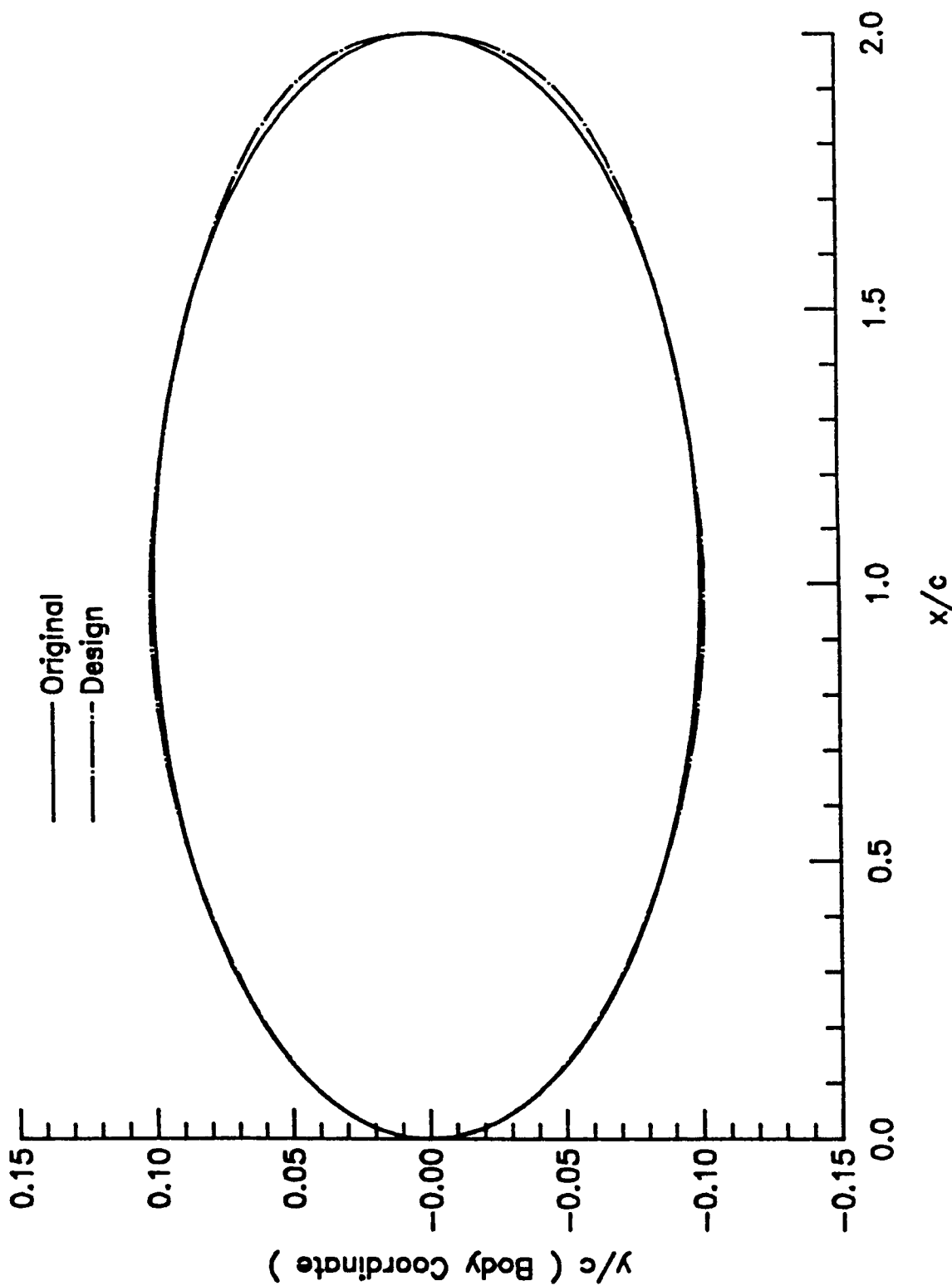
Figure 28. Comparison of Original and Design Shapes in a Nonuniform Transonic Freestream(.995−1.1)

64

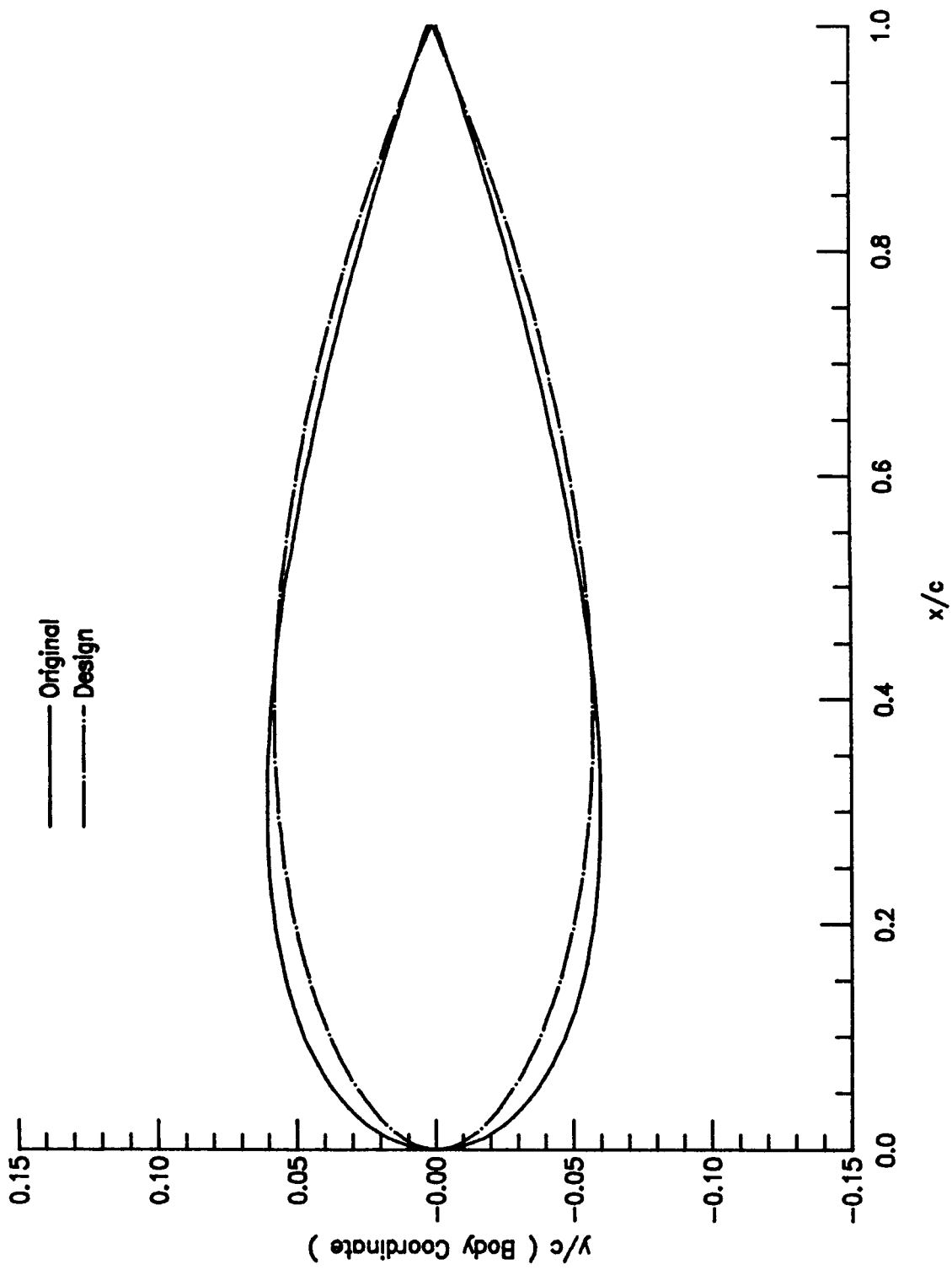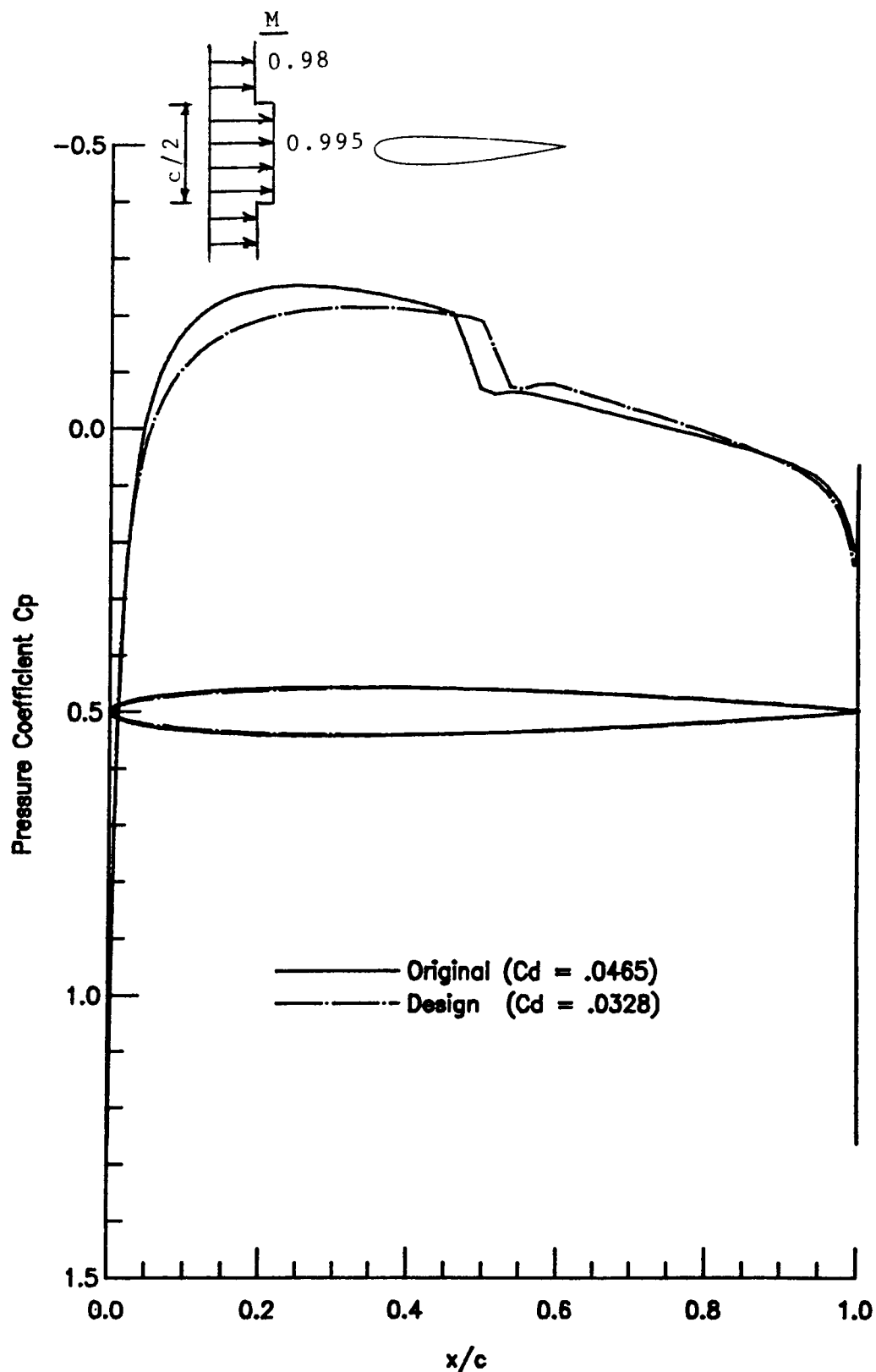Figure 29. Comparison of Original and Design Shapes and Pressure Distributions in Uniform Flow of M=0.98

Figure 30. Comparison of Original and Design Shapes in a Transonic Uniform Flow (M = 0.98)

66

Figure 31. Comparison of Original and Design Shapes and Pressure Distributions in a Transonic Nonuniform Freestream
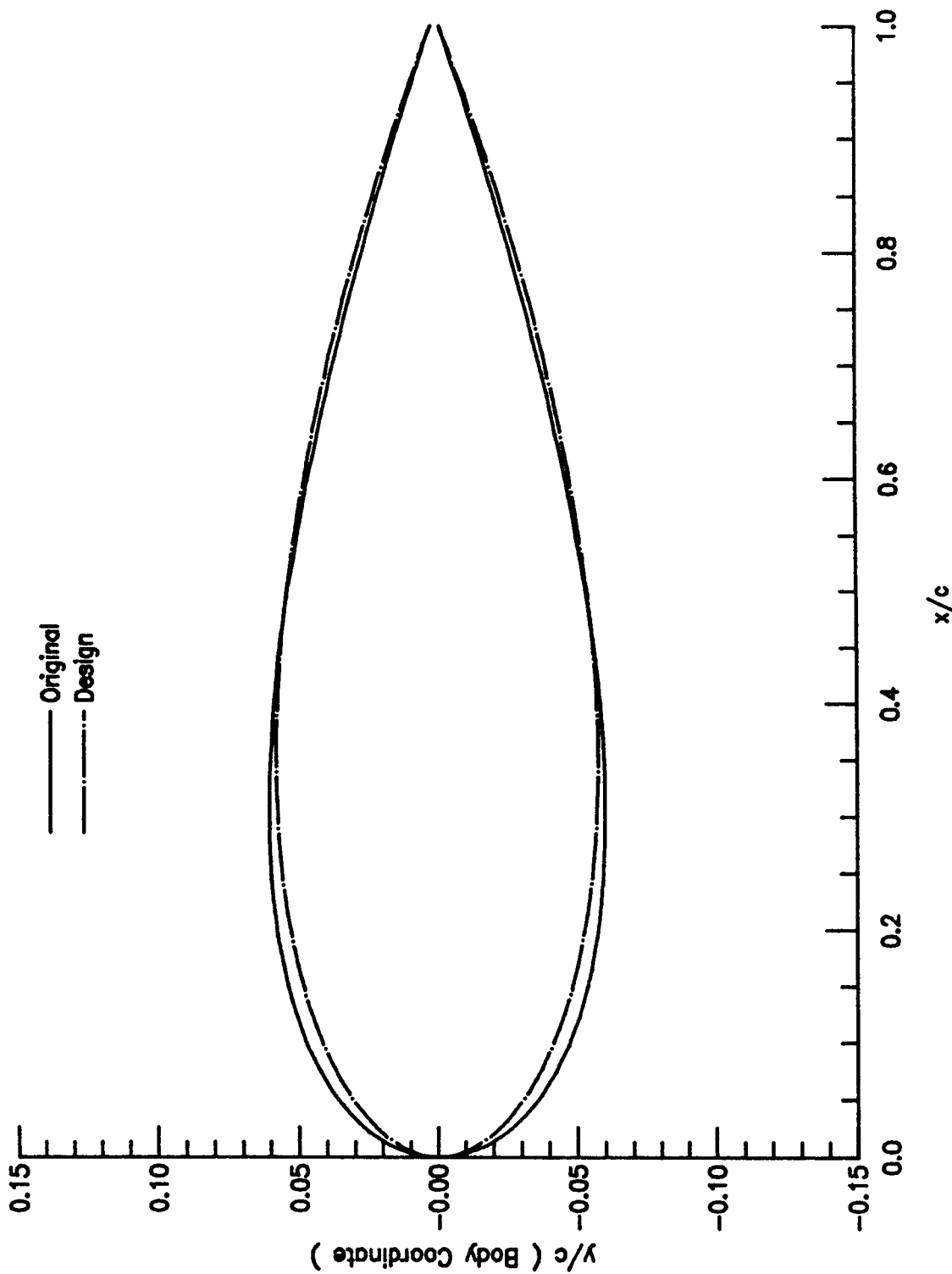
Figure 32. Comparison of Original and Design Shapes in a Nonuniform Transonic Freestream(.98-.995)

68